Nemoz, C., Ropars, V., Frit, P., Gontier, A., Drevet, P., Yu, J., Guerois, R., Pitois, A., Comte, A., Delteil, C., Barboule, N., Legrand, P., Baconnais, S., Yin, Y., Tadi, S., Barbet-Massin, E., Berger, I., Le Cam, E., Modesti, M., ... Charbonnier, J. B. (2018). XLF and APLF bind Ku80 at two remote sites to ensure DNA repair by non-homologous end joining. *Nature Structural and Molecular Biology*, *25*(10), 971-980. https://doi.org/10.1038/s41594-018-0133-6

Peer reviewed version

Link to published version (if available):
10.1038/s41594-018-0133-6

XLF and APLF bind to Ku80 on two remote sites to ensure DNA repair by non-homologous end-joining

AUTHORS

Clement Nemoz[1*], Virginie Ropars[1*], Philippe Frit[2,3*], Amandine Gontier[1], Pascal Drevet[1], Jinchao Yu[1], Raphaël Guerois[1], Aurelien Pitois[1], Audrey Comte[1], Christine Delteil[2,3], Nadia Barboule[2,3], Pierre Legrand[4], Sonia Baconnais[5], Yandong Yin[6], Satish Tadi[7], Emeline Barbet-Massin[8], Imre Berger[9], Eric Le Cam[5], Mauro Modesti[7], Eli Rothenberg[6], Patrick Calsou[2,3§], Jean-Baptiste Charbonnier[1§]

INSTITUTIONS

[1] Institute for Integrative Biology of the Cell (I2BC), Institute Joliot, CEA, CNRS, Univ. Paris-Sud, Université Paris-Saclay, 91198, Gif-sur-Yvette cedex, France

[2] Institut de Pharmacologie et Biologie Structurale, IPBS, Université de Toulouse, CNRS, UPS, Toulouse, France

[3] Equipe Labellisée Ligue Contre le Cancer 2013 and 2018

[4] Synchrotron Soleil, L'Orme des Merisiers, Saint-Aubin - BP 48, 91192 Gif-sur-Yvette Cedex, France.

[5] Signalisations, Noyaux et Innovations en Cancérologie, UMR 8126, CNRS, Université Paris-Sud, Gustave Roussy, Université Paris-Saclay, 94805 Villejuif, France.

[6] New York University School of Medicine, Perlmutter Cancer Center, USA

[7] Cancer Research Center of Marseille, CNRS UMR7258, Inserm U1068, Institut Paoli-Calmettes, Aix-Marseille Université UM105, Marseille, France.

[8] Dynamic Biosensors GmbH, Martinsried, Germany

[9] BrisSynBio Centre, The School of Biochemistry, Faculty of Biomedical Sciences, University of Bristol, Bristol, United Kingdom.

* These authors contributed equally

§ Corresponding authors : jb.charbonnier@cea.fr and calsou@ipbs.fr

ABSTRACT

The Ku70-Ku80 (Ku) heterodimer binds rapidly and tightly to ends of DNA double-strand breaks and recruits several factors of the Non-Homologous End Joining (NHEJ) pathway through molecular mechanisms that remain unclear. Here, we describe the crystal structures of the Ku-binding motifs (KBM) of the NHEJ proteins APLF (A-KBM) and XLF (X-KBM) bound to a Ku-DNA complex. The two KBMs motifs bind on remote sites of Ku80 α/β domain. The X-KBM occupies an internal pocket formed after an unprecedented large outward rotation of the Ku80 α/β domain. We reveal independent recruitment at laser-irradiated sites of the APLF-interacting protein XRCC4 and of XLF through the respective binding of A- and X-KBMs to Ku80. Finally, we show that mutations on the X-KBM and A-KBM binding sites in Ku80 compromises efficiency and accuracy of end-joining and cellular radiosensitivity. A- and X-KBMs may represent two initial anchorage points necessary to build the NHEJ intricate interactions network.

Keywords : DSB repair, NHEJ, X-ray crystallography, induced fit, laser micro-irradiation, super resolution microscopy, switchSENSE, microcalorimetry

INTRODUCTION

In mammals the majority of DNA double-strand breaks (DSBs) is repaired by the non-homologous end-joining (NHEJ) pathway [1,2]. The Ku70-Ku80 heterodimer (Ku) rapidly and tightly interacts as a preformed ring with DSBs extremities in a non-sequence specific manner [3]. Ku serves as a hub for the recruitment of several NHEJ factors [4,5]. Among them, Ku recruits the XRCC4-LIG4-XLF ligation complex through interaction with XRCC4-LIG4 [6,7] and with XLF, the latter relying on a Ku-binding motif (KBM) localized at the XLF extreme C-terminus (thereafter named X-KBM) [8,9] (Figure 1a and Supplementary Figure 1). The ligation complex organizes into filaments both *in vitro* and in cells [10-14].

Interestingly, Ku interacts also with a number of accessory NHEJ factors. The APTX and PNKP-like factor (APLF) binds poly(ADP)-ribosylated proteins near DSBs sites [15,16], and has been reported to have nuclease activity [16,17]. APLF tightly interacts with Ku through a KBM (thereafter named A-KBM) that is located in its central region [9,18] (Figure 1a and Supplementary Figure 1). This interaction has been mapped to the periphery of the Ku80 von Willebrand A domain (vWA) [5]. Ku-APLF interaction was shown to facilitate recruitment of the APLF-partner XRCC4 at damaged sites [9] and was proposed to stabilize the assembly of NHEJ factors around the DSB [19]. Notably, an A-KBM-like domain is present at the N-terminus of a recently identified inhibitor of the NHEJ pathway, CYREN(MRI), that also interacts with Ku80 [20] (Figure 1a). Ku also associates with the Werner syndrome protein (WRN) that is involved in many aspects of DNA metabolism including NHEJ [21]. Two motifs in the C-terminus of WRN cooperate for interaction with Ku, one being A-KBM like, and the other resembling the X-KBM present on XLF (Figure 1a). In addition, we and others showed recently that PAXX (Paralog of XRCC4 and XLF) interacts with the Ku70 subunit through a third type motif that is located in its C-terminus [22,23] (Figure 1a). Despite identification of KBMs in several NHEJ factors, their respective contribution to the efficiency of DSB repair is not fully understood. For example, the puzzling observations that KBM deletion in XLF or APLF depletion in human cells lead to null or intermediate repair defect deserve further investigations [9,24-27].

The interactome of Ku thus defines a large ensemble of motifs and proteins that could potentially compete or act synergistically. However, despite important structural and biophysical studies on NHEJ complexes [28], the absence of high resolution structures of Ku-

KBMs complexes limits our understanding of the roles and specificity of the different molecular interactions in the recruitment of NHEJ factors to DSBs. Mapping KBM-binding sites in structures is also needed to clarify potential competition of all the Ku interacting factors on limited positions (Supplementary figure 1).

Here, we establish the structural and functional basis of Ku unique modes of interaction with two factors within the NHEJ repair pathway. We describe the first crystal structures of Ku70-Ku80-DNA complex in interaction with the A-KBM (KBM of APLF) and with the X-KBM (KBM of XLF), revealing that the two KBMs occupy remote interaction sites on the Ku80 vWA domain. The functional context of our structural data was determined using cell based assays to visualize the recruitment of wild-type and mutant X-KBM motifs or XLF proteins as well as of the APLF-partner XRCC4 to DSBs sites induced by micro-irradiation in wild-type or mutant Ku backgrounds. Our data provide new mechanistic insights on the function of XLF and APLF in the NHEJ process.

RESULTS

The KBM of APLF tightly interacts with a highly conserved site of Ku80 vWA domain.

The APLF factor contains a conserved Ku binding motif (A-KBM, aa 179-192) (Figure 1a). We co-crystallized a 18-mer A-KBM peptide (aa 174-191) with a Ku form deleted for the C-terminal regions (Ku_{cc}), and an hairpin DNA (hDNA) [3] (Supplementary Figure 2a). In the crystal structure at 3.0 Å resolution (Table 1), the A-KBM peptide is well defined and is positioned at the periphery of the vWA domain of Ku80 (aa $T61^{80}$-$C156^{80}$) (thereafter, superscript ^{80} stands for Ku80) (Figure 1b, and Supplementary Figure 2b). It is located at more than 50 Å from the DNA binding site of Ku80. The A-KBM adopts an extended conformation in a pocket delineated by the helices α4 and α5 and the loop located between the β-strands B and C of Ku80 (Figure 1c). The hydrophobic part of the A-KBM, located in the C-terminal part of the motif, is composed by the amino acids $I_{185}LPTWML_{191}$ and is buried in a hydrophobic pocket formed by the Ku80 residues $L68^{80}$, $I112^{80}$, $M115^{80}$, $I149^{80}$ and $I150^{80}$ (Figure 1d). The N-terminal part of the A-KBM contained a patch of three consecutive basic residues and an acid residue ($E_{181}RKR_{184}$ in human sequence) (Figure 1e). It forms salt

bridges and charged hydrogen bonds with respectively the side chains of D106^{80}, D109^{80}, Q73^{80} and S145^{80}, and the main chain of K144^{80} and S143^{80}.

Isothermal Titration Calorimetry (ITC) showed that the interaction between A-KBM and Ku had a Kd of 33 ± 10 nM (Table 2, and Supplementary Figure 2e). We measured a nanomolar Kd for the interaction between Ku and a 18bp DNA as already reported [29] and found a similar Kd for the interaction between the A-KBM and Ku alone or Ku bound to a 18bp DNA (Table 2). The interaction of the A-KBM with Ku_{cc} showed Kd and enthalpy values similar to full-length Ku (KuFL). Thus, the core heterodimeric region of Ku is likely sufficient for the interaction with the A-KBM. Notably, these affinities are stronger than the ones previously reported by fluorescence polarization with a labelled A-KBM peptide (Kd of 580 nM) [9].

Mapping the conservation rate of the residues at the surface of Ku80 shows that this pocket is the main conserved pocket together with the DNA binding pocket (Figure 1f). The residues L68^{80}, Y74^{80} and I112^{80} make tight interactions with the hydrophobic part of the A-KBM motif. Mutations at these positions were reported to greatly reduce or disrupt the interactions with APLF in yeast two-hybrid experiments or in EMSA [9]. We produced the Ku I112R mutant that, as expected had no residual interaction with the A-KBM motif by ITC (Table 2).

X-KBM creates an outward rotation of the vWA domain and a large groove in Ku80.

We then determined the crystal structures of the Ku70-Ku80-hDNA complex bound with peptides derived from the XLF X-KBM ((L281^{X} to S299^{X}) and (S287^{X}-S299^{X}) peptides) (Supplementary Figure 2c). The crystal structures at 2.8 and 2.9 Å resolution (Table 1) show an unprecedented large outward rotation of the Ku80 vWA (Figure 2a, b). This movement forms a large groove between the Ku80 vWA and the rest of the Ku heterodimer. We therefore termed this conformation the open state of Ku, in contrast to the closed state observed in the three other crystal structures reported (Ku alone (1JEQ), Ku-hDNA (1JEY) and Ku-hDNA-A-KBM (this study)). The conformational change of Ku80 vWA does not affect Ku interaction with the duplex DNA (Supplementary Figure 2d)

The X-KBM is located on the Ku80 vWA face of the newly created groove in a pocket delineated by 4 strands (β_A, β_D, β_E and $\beta_{E'}$) and 3 helices (α_2, $\alpha_{7'}$, $\alpha_{7''}$). The motif is positioned

closer to the DNA (at 12Å) than the A-KBM, though not in direct contact. We can model eight residues of the X-KBM ($_{292}$KKPRGLFS$_{299}$) in the crystal obtained with the 19mer or 14mer X-KBM. These residues are the last eight residues of the XLF sequence. The residues $_{296}$GLFS$_{299}$ of the X-KBM occupy a hydrophobic pocket delineated by Ku80 residues L12^{80}, V37^{80}, F41^{80}, F135^{80}, F164^{80}, Y225^{80}, and L234^{80} (Figure 2c). In the closed state, these Ku residues are buried and mediate intramolecular contacts (Figure 2d). The X-KBM may thus stabilize a transient open conformation of Ku80 in equilibrium with the closed state under basal conditions. In addition, we observed that the Ku80 vWA opening comes along with important secondary structure changes in the linker region (R232^{80}-E241^{80}) that separates the vWA and the rest of the Ku heterodimer (Figure 2c, d).

ITC measurements showed a moderate affinity of X-KBM for Ku, with a Kd of 4.4 ± 0.2 µM (about 200-fold weaker than the affinity of the A-KBM) (Table 2, and Supplementary Figure 2f). We observed similar affinities and thermodynamic parameters for the X-KBM with a Ku-DNA complex or with Ku$_{cc}$ (Table 2). Notably, this micromolar interaction was not detected in a previous study using fluorescence polarization with labelled peptides [9]. We also measured similar affinities for the interactions between XLF homodimer and Ku alone or Ku bound to a 18bp DNA (Table 2). These data show that in absence of DNA or with a short DNA protected by Ku ring, XLF and its X-KBM interact similarly with Ku.

EMSA analyses confirmed an interaction between XLF and Ku complexed with a 50bp DNA in the µM range (Supplementary Figure 3a-b). Competitions experiments showed that the X-KBM peptide (pXLF) competes in the µM range with the XLF protein and that the A-KBM peptide (pAPLF) does not displace XLF, supporting remote sites of interactions (Figure 2e and Supplementary Figure 3c, d). Also, the C-terminus of PAXX (pPAXX) does not compete with XLF binding, in agreement with previous studies that report an interaction between PAXX C-terminus and Ku70 subunit [22,23] (Supplementary Figure 3e).

The outward rotation of the vWA domain of Ku80 is mediated by Glu133.

To evaluate if the outward rotation of Ku80 observed in the crystal structure with the X-KBM peptide was present in solution, we performed SAXS analyses. The SAXS data with the A-

KBM peptide were comparable with those of the Ku-hDNA sample without any peptide (respective Rg of 53.1Å and 53.7) (Figure 2f). We measured an increase of the Rg to 59.0Å in presence of the X-KBM, corresponding to the opening of Ku80 observed in the crystal (Figure 2f). Comparison of the Dmax values provided further corroboration for the opening of the Ku molecule with an increase of 30 Å.

The acid residue $E133^{80}$ buried in Ku80 is well positioned to act as a spring facilitating the Ku80 opening (Figure 2c, d). The glutamate $E133^{80}$ is buried in the closed conformation of the Ku80 vWA and its pKa value is estimated by the PDB2PQR-2.0 server [30] at a value of 9.1, far from the normal pKa of 4.5 for a glutamate in solvent. The outward rotation of Ku80 vWA should be energetically facilitated by the solvation of this Glu following the displacement of Ku80 residues $V236^{80}$, $F237^{80}$ and $I240^{80}$ away from $E133^{80}$ carboxylate function (Figure 2d). Multiple sequence alignments show that $E133^{80}$ position and the residues surrounding are well conserved in mammalian and saurian and that Ku70 has no equivalent buried acidic residue at this position (Supplementary Figure 4a-b).

Molecular bases of the specificities of A-KBM and X-BKM motifs binding to Ku80.

The A-KBM and X-KBM present sequence similarities with a basic patch in their N-terminus followed by a hydrophobic patch [9] (Supplementary Figure 1). Comparison of the crystal structures of Ku bound to these two motifs suggests that the high affinity of the A-KBM relies on the tryptophan $W189^{A}$ in place of the $Leu297^{X}$ in X-KBM. Thus, we used ITC to measure the interaction of the X-KBM motifs with the mutation L297W (LW) or with a non-conservative L297E mutation (LE). The (LW) peptide has a Kd of 0.12 ± 0.03 µM, an interaction 40-fold tighter than wild-type X-KBM (Table 2 and Supplementary figure 2g). The LE mutant presents no detectable interaction with Ku (Table 2). Competition experiments with Ku saturated with the A-KBM showed that the X-KBM (L297W) no longer interacts with Ku, suggesting that the sole L297W mutation is able to redirect the X-KBM towards the A-KBM binding site on Ku80 (Table 2).

Then live cell imaging was used to monitor the recruitment of CFP-fused A-KBM and X-KBM fragments to DSBs sites induced with laser micro-irradiation. Under conditions of similar damage yield (Supplementary Figure 5e), the A-KBM motif transfected in U2OS cells was strongly recruited but the W189G mutation impaired both its nuclear localization and

recruitment to laser sites (Figure 3a-b), as reported [9,18]. X-KBM live recruitment was impaired by L297E mutation but not L297W mutation (Figure 3c), corroborating ITC data. We then used U2OS cells expressing an inducible shRNA against Ku80 [31] (Supplementary Figure 5a) that were complemented with wild-type or I112R mutant Ku80 (Supplementary Figure 5c-d). The I112R mutation impaired A-KBM recruitment, as expected, but not that of X-KBM (Figure 3d, e). Notably, I112R Ku80 mutant specifically lowered the recruitment of L297W X-KBM (compare Figures 3c and 3f). Conversely, APLF knock-down boosted the recruitment of the LW mutant peptide above that of wild-type X-KBM (Figure 3g and Supplementary Figure 5b for control of shAPLF efficiency). Together, these data in cells support that the LW mutation redirects the X-KBM fragment to the APLF-binding site in Ku80 and point out the W189 residue as a key determinant for APLF specific interaction with Ku80.

X-KBM mutations impair XLF recruitment and XRCC4-XLF filament stability.

We then investigated the properties of the interaction between full-length XLF protein and Ku. We first used the SwitchSENSE approach [32] in which oligonucleotide nanolevers labelled with a fluorescence probe are bound to a gold surface (Supplementary Figure 3f). Ku bound onto 48bp DNA nanolevers with a Kd in the nM range as already reported [29] and a long dissociation time (Supplementary Figure 3g). Wild-type XLF onto the Ku-DNA complex showed a rapid k_{on} ($4.7 \pm 1.7\ 10^5\ M^{-1}s^{-1}$) followed by a rapid dissociation ($k_{off} = 0{,}09 \pm 0{,}004\ s^{-1}$) and a corresponding Kd of 0.19 ± 0.07 µM (Figure 4a). This affinity is about 10 fold stronger than the one measured by ITC with a smaller DNA and may reflect additional interactions of XLF with DNA emerging from Ku ring as observed with PAXX [22]. LW and LE mutants showed a 2.3- and 5.1-fold weaker affinity than WT protein, respectively (Kd of 0.45 ± 0.26 µM for LW and Kd of 0.98 ± 0.15 µM for LE) (Supplementary Figure 3h). As compared with ITC and recruitment data with X-KBM LW mutant peptide, this suggests that the LW mutation cannot redirect the XLF protein to the APLF binding site in Ku80.

We then measured the recruitment of the CFP-tagged full-length XLF protein (CFP-XLF) expressed in human XLF-defective BuS cells (SV40T-transformed, telomerase immortalized fibroblasts derived from the XLF-deficient P2 patient - homozygous C622T nonsense mutant (R178X)) [33] (Figure 4b). Wild-type XLF showed a rapid mobilization to irradiated nuclear

sites, as reported [34]. Both LE and LW mutations impaired to various extents XLF protein recruitment (Figure 4b), again indicating that LW mutation cannot redirect the XLF protein to the APLF binding site in Ku80. In addition, we observed an important reduction of the recruitment of G296W, S299E or F298G XLF mutants in the extreme C-terminus (Supplementary Figure 5f-h). We also questioned the contribution of APLF-XRCC4 complex to XLF recruitment by expressing L115D XLF mutant unable to interact with XRCC4 [35,36]. We measured an efficient recruitment of L115D XLF to laser-induced DSBs that was insensitive to APLF knock-down but impaired with the XLF L115D/L297E XLF double mutant (Supplementary Figure 5i). Together, these data support a major role for Ku80 interaction with L297 and extreme C-terminal residues for XLF recruitment at DSBs in cells.

Multi-color super-resolution localization microscopy (STORM) allows characterizing formation of XRCC4-XLF filaments close to Ku foci and DSBs ends [14]. On DSBs induction with the radiomimetic drug neocarzinostatin, extended XLF filaments close to Ku80 foci were observed in XLF complemented BuS cells, whereas cells harboring (LE) and (LW) mutants showed slightly smaller and more punctuated XLF structures (Figure 4c and Figure 4d-e for quantification). In contrast to these data, evaluation of the effect of mutations in the X-KBM on cell radiosensitivity showed that (LW) or (LE) XLF mutants were associated with respectively no or minor radiosensitization, compared to high radiosensitivity of BuS cells and full restoration of radioresistance on expression of wild-type XLF (Figure 4f).

APLF and XLF binding to Ku80 promote DSB repair and cell survival to IR.

Finally, we questioned the discrepancy between subnormal cell survival and defective XLF recruitment and filaments formation associated with mutations in X-KBM. The outward rotation in Ku80 upon X-KBM binding more likely relies on $E133^{80}$, the equivalent position of which in Ku70 is a methionine (M167) (Supplementary Figure 4b). Therefore, we designed E133M mutant in Ku80 and Q162E mutation that may alter the charge environment of E133 (Supplementary Figure 5c). E133M or Q162E mutation in Ku80 negatively impacted X-KBM recruitment but not that of control A-KBM (Supplementary Figures 6a and 6b). This result further supports the independent binding sites on Ku80 of the A-KBM and X-KBM motifs and validates E133 and Q162 positions in Ku80 as key residues for X-KBM binding.

Then, mutations in the Ku80 binding sites for X- and A-KBM were combined in the I112R/E133M Ku80 double mutant (Supplementary Figure 5d). This combination of mutations clearly impaired the recruitment of both CFP-(X- and A-KBM) peptides (Figures 5a and 5b) while the recruitment of the mutant CFP-Ku fusions was preserved (Supplementary Figure 6c-d). We also measured the recruitment of the APLF partner XRCC4 and of XLF, expressed as CFP-tagged full-length proteins (Figure 5c-d). Strikingly, only the double E133M/I112R mutation strongly but not completely impaired the recruitment of both proteins (Figure 5c-d). This result supports the independent binding of APLF-XRCC4 and XLF proteins on Ku80.

Ku80 mutants expressed in U2OS cells had no detectable impact on XLF filaments (Supplementary Figure 6e-f) but lowered end-joining efficiency on a linear plasmid transfected in U2OS cells (Figure 5e). To assess repair accuracy, we used an assay in which GFP expression from a cassette integrated in cells relied on the loss of a DNA fragment between two cut sites (modified from [37]) (Figure 5f), reported to be favoured upon NHEJ inhibition [38,39]. Strikingly, we observed an increase in fragment loss with the three Ku80 mutants (Figure 5f), indicating that loose APLF-XRCC4 or XLF interactions with Ku80 promote genomic instability. Finally, the combination of E113M and I112R Ku80 mutations had a strong impact on cell radiosensitivity with an additive effect of both mutations (Figure 5g). These results indicate that APLF-XRCC4 and XLF interactions with Ku80 cooperate to promote cell survival to IR.

DISCUSSION

Here, we show that each of the A- and X-KBM binds Ku independently of other APLF or XLF protein domains. This is in contrast with the absence of binding reported for the isolated X-KBM in recent studies with fluorescent polarization [9,40] that may be due to lower sensitivity, steric hindrance by the fluorescence probe or differences in the Ku constructs used. Therefore, the present results rule out the conclusion that Ku-XLF interaction necessarily needs XLF binding to DNA (even though DNA could stabilise the interaction, as deduced from our switchSENSE data) or to DNA-PKcs [40].

Despite the A-KBM and X-KBM motifs have important sequence similarities (Supplementary figure 1), they target different regions of Ku80 with different modes of actions, a more rigid one for the A-KBM and an induced fit one for the X-KBM. In contrast to the L297W X-KBM peptide, the (LW) full-length XLF mutant protein cannot be redirected to the APLF-binding site on Ku80. This may be explained by steric constraints either intrinsic to the protein structure or due to interactions with other partners in the NHEJ complex. It was reported that a X-KBM in WRN protein functions cooperatively with an A-KBM located upstream (1403-1412) in binding Ku complexes [40] (Figure 1a). Our structural data allow proposing the first model of Ku interacting with the tandem sequence of the WRN A-KBM and X-KBM, including the central linker (Supplementary Figure 4c). This model now awaits validation by the crystal structure of the tandem motif of WRN on Ku.

XRCC4 and XLF organize into filaments both *in vitro* and in cells [10-14] and can also assemble as sliding sleeves-like structures on broken DNA *in vitro* even without Ku [41]. In this study, cells containing single or double mutations on the A-KBM and/or X-KBM binding sites of Ku80 show intact filaments while mutations on the X-KBM of XLF induce a slight reduction in the filaments size. These data suggest that interactions additional to Ku80-XLF may participate in filament formation, like the XLF C-terminal DNA-binding domain that spans the X-KBM [42].

How is NHEJ ligation complex assembled at broken DNA? APLF FHA domain interacts with XRCC4 [17,26] and XLF establishes head to head contact with XRCC4 [10-13]. Here, we show that the two remote APLF- and XLF-KBM binding sites in Ku80 promote the independent recruitment of XRCC4 and XLF at broken DNA and that disruption of XRCC4-XLF interaction (through L115D mutation) does not compromise XLF recruitment. Destabilisation of APLF or XLF interactions with Ku80 impairs repair efficiency and cell survival to DSBs and also favours genome instability associated with distal end-joining. These effects are most likely explained by loose assembly of the NHEJ apparatus at break ends. Therefore, we propose a model in which APLF and XLF KBMs represent two initial anchorage points for the rapid and independent recruitment of APLF-XRCC4 and XLF on Ku (Figure 5h). After initial recruitment, interactions additional to Ku80-XLF contacts may stabilize XLF at DBS sites (Figure 5h): our recruitment data show a stable interaction of XLF at DSB sites in cells that differs from the rapid dissociation from Ku-DNA observed *in vitro* by switchSENSE; also, although XRCC4 is dispensable for XLF initial recruitment, it has been shown to

stabilize XLF at damaged sites [34]. Thus, additional contacts stabilizing XLF may include XLF-DNA [34,42,43] and/or XLF-XRCC4 interactions, including filaments formation [10-14] and/or interaction with the LIG4 BRCT1 domain [44]. In addition, after XRCC4 recruitment through APLF binding to Ku, XRCC4 may also stabilize in turn APLF at damaged sites since FHA mutants of APLF that do not interact with XRCC4 show a reduced retention after laser micro-irradiation [18]. Moreover, links with DNA-PK may further properly stabilize and/or position the NHEJ ligation complex at DSBs (Figure 5h): Ku directly interacts with the XRCC4-LIG4 complex [7] through either XRCC4 [45] or LIG4 [6] and DNA-PKcs also directly contacts XRCC4 [46-48]. Intimate links between the DNA-PK and ligation complexes are illustrated by the requirement of an intact XLF-XRCC4-LIG4 complex to ensure optimal DNA ends synapsis [49,50].

The intricate network linking end-recognition and ligation NHEJ complexes may allow compensation of partially defective individual components. Indeed, we found that separate or even combined Ku80 mutations do not completely abolish XRCC4 and XLF recruitment and do not radiosensitize cells as much as XLF complete defect that abolishes all XLF functions in NHEJ [51]. In that view, only a mild, if any, repair defect in human cells has been associated with X-KBM deletion [27] or APLF depletion [9,24-26]: in case of individual absence of XLF C-terminal tail or of APLF, the other intact partner would still bind to Ku80 and be able, although with a slower kinetics, to recruit the other components to achieve ligation.

Finally, our present study adds a new aspect to the DNA-PK-ligation complex interaction network that is the swing of the Ku80 vWA domain upon XLF binding (Figure 5h). From our structural and mutagenesis approaches, we propose that the outward swing of the vWA domain of Ku80 is mainly dependent on the conserved acidic residue $E133^{80}$. Although this swing does not impact the A-KBM binding site nor the DNA binding domain, it exposes a large groove between the vWA and the ring domain of Ku80 that may non-exclusively reinforce XRCC4-LIG4 and/or XLF interaction with Ku or attract yet unknown components. Interestingly, XLF deficiency impacts on the activity of the Ku partner terminal deoxynucleotidyl transferase during V(D)J recombination [52]. Mutagenesis studies on the conserved positions that delineated the unmasked surface of this groove will help to define precisely the role of this swing in the NHEJ reaction.

In conclusion, the present data further substantiate the emerging model that several NHEJ factors bearing a limited repertoire of KBMs recognize a limited number of KBM-binding sites on Ku [16]. The complex regulation of Ku sites occupancy by NHEJ factors during the repair process deserves further investigations.

ACCESSION CODES. Crystal structures are deposited at the pdb with the following codes Ku-DNA-pAPLF (6ERF), Ku-DNA-pXLF (6ERH) and Ku-DNA-pXLFshort (6ERG)

ACKNOWLEDGMENTS

J-B.C is supported by ARC program (SLS220120605310), ANR (ANR-12-SVSE8-012), INCA DomRep (PLBIO 2012-280), CEFIPRA grant 5203C and by the French Infrastructure for Integrated Structural Biology (FRISBI) ANR-10-INBS-05. Work in E.R's laboratory is supported by National Institutes of Health Grants CA187612, GM108119, and the American Cancer Society RSG DMC-16-241-01-DMC. P.C's team is supported by the Ligue Nationale Contre Le Cancer (Equipe labellisée 2013 and 2018) and Electricité de France (EDF, Conseil de Radioprotection). J-B.C, M.M and P.C are supported by ANR (CE12 2017 NHEJLIG4 grant). We thank K.W. Caldecott (University of Sussex, Brighton, UK) for the gift of anti-APLF antibody and J.M. Stark (City of Hope, Duarte, USA) for the gift of U2OS cells engineered with the integrated distal-end-joining reporter. We would like to thank the Imaging Core Facility TRI-IPBS, in particular S. Mazeres and R. Poincloux for maintenance of the live-cell microscopy equipment and E. Näser for the maintenance of the flow-cytometers. Flow-cytometry equipment was with the financial support from ITMO Cancer Aviesan (Alliance Nationale Pour les Sciences de la Vie et de la Santé, National Alliance for Life Science and Health) within the framework of Cancer Plan. We thank J-P. de Villartay and F. Theillet for careful reading of the manuscript.

AUTHORS CONTRIBUTIONS

P.C. and J-B.C conceived this study. C.N, V.R, A.G, A.P, A.C, S.B expressed and purified recombinant proteins with help from P.D, E.L.C and I.B. C.N and V.R produced crystals and collected crystallographic data with help from P.L. C.N, V.R, P.L and J-B.C carried out the crystallographic analysis and interpreted the results. C.N, A.G, S.B, E.L.C and J-B.C designed, performed, and analyzed microcalorimetry and biophysical experiments. E.B-M, A.C and J-B.C designed, performed, and analyzed switchSENSE experiments. S.T and M.M

designed, performed, and analyzed electromobility shift assays. P.F and P.C designed and constructed vectors and cell lines for life cell imaging and radiosensitivity. P.F, C.D, N.B and P.C designed, performed and analyzed western blot analyses of Ku variants, life cell imaging, DNA repair and radiosensitivity experiments. Y.Y and E.R designed, performed and analyzed the super resolution microscopy. J.Y and R.G performed bioinformatic analyses. All the authors discussed the data. C.N, P.C and J-B.C wrote the manuscript with input from V.R, P.F, P.D, R.G, M.M, E.B-M, Y.Y and E.R.

COMPETING FINANCIAL INTERESTS

The authors declare no competing financial interests.

REFERENCES

1. Lieber, M.R. The Mechanism of Double-Strand DNA Break Repair by the Nonhomologous DNA End-Joining Pathway. *Annu Rev Biochem* **79**, 181-211 (2010).
2. Chang, H.H.Y., Pannunzio, N.R., Adachi, N. & Lieber, M.R. Non-homologous DNA end joining and alternative pathways to double-strand break repair. *Nat Rev Mol Cell Biol* **18**, 495-506 (2017).
3. Walker, J.R., Corpina, R.A. & Goldberg, J. Structure of the Ku heterodimer bound to DNA and its implications for double-strand break repair. *Nature* **412**, 607-14 (2001).
4. Grundy, G.J., Moulding, H.A., Caldecott, K.W. & Rulten, S.L. One ring to bring them all-The role of Ku in mammalian non-homologous end joining. *DNA Repair (Amst)* **17**, 30-8 (2014).
5. Rulten, S.L. & Grundy, G.J. Non-homologous end joining: Common interaction sites and exchange of multiple factors in the DNA repair process. *Bioessays* **39**(2017).
6. Costantini, S., Woodbine, L., Andreoli, L., Jeggo, P.A. & Vindigni, A. Interaction of the Ku heterodimer with the DNA ligase IV/Xrcc4 complex and its regulation by DNA-PK. *DNA Repair (Amst)* **6**, 712-22 (2007).
7. Nick McElhinny, S.A., Snowden, C.M., McCarville, J. & Ramsden, D.A. Ku recruits the XRCC4-ligase IV complex to DNA ends. *Mol Cell Biol* **20**, 2996-3003 (2000).
8. Yano, K.I., Morotomi-Yano, K., Lee, K.J. & Chen, D.J. Functional significance of the interaction with Ku in DNA double-strand break recognition of XLF. *FEBS Lett* **585**, 841-6 (2011).
9. Grundy, G.J. et al. APLF promotes the assembly and activity of non-homologous end joining protein complexes. *Embo J* **32**, 112-25 (2013).
10. Ropars, V. et al. Structural characterization of filaments formed by human Xrcc4-Cernunnos/XLF complex involved in nonhomologous DNA end-joining. *Proc Natl Acad Sci U S A* **108**, 12663-8 (2011).
11. Hammel, M. et al. XRCC4 interactions with XRCC4-like factor (XLF) create an extended grooved scaffold for DNA ligation and double-strand break repair. *J Biol Chem* **286**, 32638-50 (2011).
12. Andres, S.N. et al. A human XRCC4-XLF complex bridges DNA. *Nucleic Acids Res* **40**, 1868-78 (2012).

13. Wu, Q. et al. Non-homologous end-joining partners in a helical dance: structural studies of XLF-XRCC4 interactions. *Biochem Soc Trans* **39**, 1387-92 (2011).
14. Reid, D.A. et al. Organization and dynamics of the nonhomologous end-joining machinery during DNA double-strand break repair. *Proc Natl Acad Sci U S A* **112**, E2575-84 (2015).
15. Ahel, I. et al. Poly(ADP-ribose)-binding zinc finger motifs in DNA repair/checkpoint proteins. *Nature* **451**, 81-5 (2008).
16. Rulten, S.L., Cortes-Ledesma, F., Guo, L., Iles, N.J. & Caldecott, K.W. APLF (C2orf13) is a novel component of poly(ADP-ribose) signaling in mammalian cells. *Mol Cell Biol* **28**, 4620-8 (2008).
17. Kanno, S. et al. A novel human AP endonuclease with conserved zinc-finger-like motifs involved in DNA strand break responses. *Embo J* **26**, 2094-103 (2007).
18. Shirodkar, P., Fenton, A.L., Meng, L. & Koch, C.A. Identification and functional characterization of a Ku-binding motif in Aprataxin Polynucleotide kinase/phosphatase-Like Factor (APLF). *J Biol Chem* **288**, 19604-13 (2013).
19. Hammel, M. et al. An Intrinsically Disordered APLF Links Ku, DNA-PKcs, and XRCC4-DNA Ligase IV in an Extended Flexible Non-homologous End Joining Complex. *J Biol Chem* **291**, 26987-27006 (2016).
20. Arnoult, N. et al. Regulation of DNA repair pathway choice in S and G2 phases by the NHEJ inhibitor CYREN. *Nature* **549**, 548-552 (2017).
21. Rossi, M.L., Ghosh, A.K. & Bohr, V.A. Roles of Werner syndrome protein in protection of genome integrity. *DNA Repair (Amst)* **9**, 331-44 (2010).
22. Tadi, S.K. et al. PAXX Is an Accessory c-NHEJ Factor that Associates with Ku70 and Has Overlapping Functions with XLF. *Cell Rep* **17**, 541-555 (2016).
23. Ochi, T. et al. DNA repair. PAXX, a paralog of XRCC4 and XLF, interacts with Ku to promote DNA double-strand break repair. *Science* **347**, 185-8 (2015).
24. Bekker-Jensen, S. et al. Human Xip1 (C2ORF13) is a novel regulator of cellular responses to DNA strand breaks. *J Biol Chem* **282**, 19638-43 (2007).
25. Iles, N., Rulten, S., El-Khamisy, S.F. & Caldecott, K.W. APLF (C2orf13) is a novel human protein involved in the cellular response to chromosomal DNA strand breaks. *Mol Cell Biol* **27**, 3793-803 (2007).
26. Macrae, C.J., McCulloch, R.D., Ylanko, J., Durocher, D. & Koch, C.A. APLF (C2orf13) facilitates nonhomologous end-joining and undergoes ATM-dependent hyperphosphorylation following ionizing radiation. *DNA Repair (Amst)* **7**, 292-302 (2008).
27. Malivert, L. et al. The C-terminal domain of Cernunnos/XLF is dispensable for DNA repair in vivo. *Mol Cell Biol* **29**, 1116-22 (2009).
28. Brosey, C.A., Ahmed, Z., Lees-Miller, S.P. & Tainer, J.A. What Combined Measurements From Structures and Imaging Tell Us About DNA Damage Responses. *Methods Enzymol* **592**, 417-455 (2017).
29. Blier, P.R., Griffith, A.J., Craft, J. & Hardin, J.A. Binding of Ku protein to DNA. Measurement of affinity for ends and demonstration of binding to nicks. *J Biol Chem* **268**, 7594-601 (1993).
30. Dolinsky, T.J. et al. PDB2PQR: expanding and upgrading automated preparation of biomolecular structures for molecular simulations. *Nucleic Acids Res* **35**, W522-5 (2007).
31. Cheng, Q. et al. Ku counteracts mobilization of PARP1 and MRN in chromatin damaged with DNA double-strand breaks. *Nucleic Acids Res* **39**, 9605-9619 (2011).
32. Langer, A. et al. Protein analysis by time-resolved measurements with an electro-switchable DNA chip. *Nat Commun* **4**, 2099 (2013).

33. Buck, D. et al. Cernunnos, a novel nonhomologous end-joining factor, is mutated in human immunodeficiency with microcephaly. *Cell* **124**, 287-99 (2006).
34. Yano, K.I. & Chen, D.J. Live cell imaging of XLF and XRCC4 reveals a novel view of protein assembly in the non-homologous end-joining pathway. *Cell Cycle* **7**, 1321-5 (2008).
35. Hammel, M., Yu, Y., Fang, S., Lees-Miller, S.P. & Tainer, J.A. XLF Regulates Filament Architecture of the XRCC4.Ligase IV Complex. *Structure* **18**, 1431-42 (2010).
36. Malivert, L. et al. Delineation of the XRCC4 interacting region in the globular head domain of cernunnos/XLF. *J Biol Chem* **285**, 26475-83 (2010).
37. Bennardo, N., Cheng, A., Huang, N. & Stark, J.M. Alternative-NHEJ Is a Mechanistically Distinct Pathway of Mammalian Chromosome Break Repair. *PLoS Genet* **4**, e1000110 (2008).
38. Bennardo, N., Gunn, A., Cheng, A., Hasty, P. & Stark, J.M. Limiting the persistence of a chromosome break diminishes its mutagenic potential. *PLoS Genet* **5**, e1000683 (2009).
39. Gunn, A., Bennardo, N., Cheng, A. & Stark, J.M. Correct end use during end joining of multiple chromosomal double-strand breaks is influenced by repair protein RAD50, DNA-dependent protein kinase DNA-PKcs, and transcription context. *J Biol Chem* **286**, 42470-82 (2011).
40. Grundy, G.J. et al. The Ku-binding motif is a conserved module for recruitment and stimulation of non-homologous end-joining proteins. *Nat Commun* **7**, 11242 (2016).
41. Brouwer, I. et al. Sliding sleeves of XRCC4-XLF bridge DNA and connect fragments of broken DNA. *Nature* **535**, 566-9 (2016).
42. Andres, S.N., Modesti, M., Tsai, C.J., Chu, G. & Junop, M.S. Crystal Structure of Human XLF: A Twist in Nonhomologous DNA End-Joining. *Mol Cell* **28**, 1093-101 (2007).
43. Lu, H., Pannicke, U., Schwarz, K. & Lieber, M.R. Length-dependent binding of human XLF to DNA and stimulation of XRCC4: DNA ligase IV activity. *J Biol Chem* **282**, 11155-62 (2007).
44. Wu, P.Y. et al. Interplay between cernunnos-XLF and NHEJ proteins at DNA ends in the cell. *J Biol Chem* **282**, 31937-43 (2007).
45. Mari, P.O. et al. Dynamic assembly of end-joining complexes requires interaction between Ku70/80 and XRCC4. *Proc Natl Acad Sci U S A* **103**, 18597-602 (2006).
46. Hsu, H.L., Yannone, S.M. & Chen, D.J. Defining interactions between DNA-PK and ligase IV/XRCC4. *DNA Repair (Amst)* **1**, 225-35 (2002).
47. Leber, R., Wise, T.W., Mizuta, R. & Meek, K. The XRCC4 gene product is a target for and interacts with the DNA-dependent protein kinase. *J Biol Chem* **273**, 1794-801 (1998).
48. Wang, Y.G., Nnakwe, C., Lane, W.S., Modesti, M. & Frank, K.M. Phosphorylation and regulation of DNA ligase IV stability by DNA-dependent protein kinase. *J Biol Chem* **279**, 37282-90 (2004).
49. Cottarel, J. et al. A noncatalytic function of the ligation complex during nonhomologous end joining. *J Cell Biol* **200**, 173-86 (2013).
50. Graham, T.G., Walter, J.C. & Loparo, J.J. Two-Stage Synapsis of DNA Ends during Non-homologous End Joining. *Mol Cell* **61**, 850-8 (2016).
51. Menon, V. & Povirk, L.F. XLF/Cernunnos: An important but puzzling participant in the nonhomologous end joining DNA repair pathway. *DNA Repair (Amst)* **58**, 29-37 (2017).

52. Jspeert, H. et al. XLF deficiency results in reduced N-nucleotide addition during V(D)J recombination. *Blood* **128**, 650-9 (2016).

FIGURE LEGENDS

Figure 1. Crystal structure of the APLF KBM (A-KBM) bound to the Ku80 vWA domain.

(a) Positions of the A-KBM (magenta) and X-KBM (blue) motifs in APLF, XLF, WRN and CYREN. The C-terminal domain of PAXX contains a P-KBM that interacts with Ku70 subunit. NTD: N-terminal domain. **(b)** Overall view of the quaternary complex Ku70/Ku80/hDNA/(APLF peptide). The A-KBM (magenta) binds at the periphery of the Ku80 (light green) vWA domain. The Ku70 subunit and hDNA are represented respectively in orange and red. The hairpin part of the DNA has been removed for clarity. **(c)** The N-terminal part of the A-KBM motif has an extended conformation whereas the C-terminal residues form a turn. **(d-e)** Zoom of the interactions made by (d) the hydrophobic patch and (e) the basic patch of the A-KBM. (**f**) The A-KBM binding site is delineated by conserved residues of Ku80 vWA domain. The binding site is represented in surface mode with amino acids colored according to their conservation rate: red (highly conserved) to white (not conserved)). The conservation rate was measured using sequences of metazoan Ku80. The orientation is the same as in (c).

Figure 2. Crystal structure of the XPLF KBM (X-KBM) bound to the Ku80.

(a) Crystal structure of the quaternary complex Ku70-Ku80-DNA-(X-KBM peptide). The X-KBM (blue) binds in an internal site of the Ku80 subunit created upon an outward rotation of the vWA domain. The Ku80 vWA opening creates a large groove between the Ku80 vWA and the rest of the heterodimer. **(b)** The crystal structure of Ku70/Ku80/DNA in presence of the A-KBM is shown with the same orientation. **(c-d)** Comparison of the X-KBM binding site in presence of X-KBM (c) or A-KBM (d) peptides. The X-KBM interacts with Ku80 residues involved in Ku intramolecular contacts in the closed state of Ku observed with the A-KBM or with no peptide. The last GLFS residues of the X-KBM interact with the bottom of the groove formed in the open state. The glutamic acid presents an atypical hydrophobic environment and could be at the origin of the vWA instability. The X-KBM residues occupy the position of

598 the helix 236-241 of Ku80 in the closed conformation and some X-KBM side chains ($R295^X$,
599 $L297^X$ and $F298^X$) mimic the intramolecular interactions made by Ku80 residues with the
600 vWA domain. **(e)** Gel shift assay with XLF and Ku in presence of a 50bp DNA with a FAM
601 in 5'and competition with pXLF containing the X-KBM motif. The arrow indicates the XLF-
602 Ku-DNA complex. Uncropped gel image is shown in Supplementary Data Set 1. **(f)** The pair
603 distributions P(r) obtained in solution by SAXS analysis indicates an opening of the
604 Ku70/Ku80/DNA complex with higher Dmax and Rg in presence of the X-KBM (blue line)
605 compared to the Ku/DNA complex without peptide (grey line) and to the A-KBM complex
606 (magenta line). Values deduced from SAXS analysis are reported beside the curves.
607
608
609 **Figure 3. Life cell imaging of A-KBM and X-KBM recruitment after nuclear micro-**
610 **irradiation.**
611 **(a)** Wild-type (WT) and mutant CFP-(A-KBM) behaviour at 0 s and 50 s after laser nuclear
612 micro-irradiation. The white rectangle and arrows mark irradiated areas. Magnification: X40.
613 **(b)** Dynamics of wild-type and mutant CFP-(A-KBM) at laser-induced damage sites in U2OS
614 cells. Mean values of relative fluorescence with s.e.m. were calculated from data obtained in
615 several individual cells: n=23 and 19 cells for WT and mutant A-KBM, respectively). *p*
616 values at last time point were calculated using unpaired two-tailed *t*-test: WT *vs* W189G
617 $p<0.0001$. **(c)** Dynamics of wild-type and mutant CFP-(X-KBM) at laser-damaged sites as in
618 b). n=27, 21, and 24 cells for WT, L297E and L297W X-KBM, respectively. *p* values at last
619 time point : WT *vs* L297W $p=0.8574$; WT *vs* L297E $p=0.0021$. (**d-e)** Dynamics of CFP-(A-
620 KBM) (d) and (X-KBM) (e) at laser damaged sites in cells expressing wild-type or I122R
621 mutant Ku80 as in b). n=20, 13 cells for A-KBM in WT or I122R Ku80, and n=48 and 39
622 cells for X-KBM in WT or I122R Ku80, respectively. *p* values at last time point : (d) WT *vs*
623 I112R $p=0.0002$; (e) WT *vs* I112R $p=0.5692$ **(f-g)** Dynamics of wild-type and mutant CFP-
624 (X-KBM) at laser-damaged sites in cells expressing I112R mutant Ku80 (f) or treated with a
625 shAPLF (g) as in b). n=26, 28, and 21 cells for WT, L297E and L297W X-KBM in (f), and
626 n=15 cells for each of WT, L297E and L297W X-KBM in (g). *p* values at last time point : (f)
627 WT *vs* L297W $p=0.023$; WT *vs* L297E $p=<0.0001$; (g) WT *vs* L297W $p=0.0144$; WT *vs*
628 L297E $p=0.2654$.
629
630

Figure 4. Biophysical and cellular analyses of XLF mutants in X-KBM.

(a) SwitchSENSE kinetic analysis of the WT XLF interaction with Ku-DNA complexes. Solid grey lines represent raw data (from 1 to 8 μM; light grey to dark grey; averages of triplicates). Global fitting was performed, following a single-exponential function (solid orange lines) yielding kinetic rate constants; k_{ON}=4.7 ± 1.7 10^5 $M^{-1}s^{-1}$ and k_{OFF} = 9.1 ± 0.4 10^{-2} s^{-1} for XLF(wt). **(b)** Dynamics of wild-type and mutant CFP-XLF at laser-damaged sites in BuS cells as in Figure 3b. n=20 cells for WT, L297E and L297W XLF. *p* values at last time point : WT *vs* L297W p=0.0093; WT *vs* L297E p<0.0001. **(c)** Representative super-resolution images of WT, L297E mutant, and L297W mutant BuS nucleus, with XLF and Ku displayed in green and magenta, respectively (scale = 2500 nm). Right: zoomed-in areas (scale = 250 nm). **(d)** Representative pair correlation function calculated from the 8x8 μm^2 center square of one XLF nucleus image of WT (green), L297E (red), and L297W (blue) mutants. WT XLF shows bigger correlation radius (arrow). **(e)** Statistics of XLF foci size. Each plot represents the average XLF foci size (indicated as radius translated from the correlation radius) in one nucleus. Box's height displays the s.d. with the mean value labelled in the middle. n=116, 95, 104 nuclei for WT, L297E, and L297W. The two-sample unpaired *t*-test between WT and L297E is p=10^{-13} while that between WT and L297W is p=0.03. **(f)** Cell survival of BuS cells complemented with vector (EV) or WT or mutated XLF. y axis is log scale. Error bars represent s.d., n=5 to 6 independent experiments. *p* values were calculated using unpaired two-tailed *t*-test: WT *vs* EV p=1.788e-06 ; WT *vs* LW p=0.068 ; WT *vs* LE p=0.021. Significant *p*-values are indicated as follows: *p< 0.05, **p < 0.01, ***p < 0.001.

Figure 5. Effects of Ku80 mutations in APLF and XLF binding sites.

(a-b) Dynamics of CFP-(A-KBM) (a) and (X-KBM) (b) at laser damaged sites as in Figure 3b, in U2OS cells expressing wild-type or I112R/E133M mutant Ku80. n=20 and 9 cells for WT and mutant Ku80 in (a) and n=48 and 11 cells for WT and mutant Ku80 in (b). *p* values at last time point: (a) WT *vs* I112R/E133M p=0.001; (b) WT *vs* I112R/E133M p=0.0111. **(c-d)** Dynamics of CFP-XRCC4 (c) and XLF (d) at laser-damaged sites in cells expressing wild-type, I112R, E133M or I112R/E133M mutant Ku80. n=38, 27, 28, and 24 cells for WT, E133M, I112R and I112R/E133M Ku80 conditions in (c) and n=24, 26, 20 and 23 cells for I112R, WT, I112R/E133M and E133M Ku80 conditions in (d). *p* values at last time point: (c) WT *vs* E133M p=0.532; WT *vs* I112R p=0.0133; WT *vs* I112R/E133M p=0.0048; (d) WT *vs* I112R p=0.246; WT *vs* E133M p=0.0048; WT *vs* I112R/E133M p=0.0248. **(e)** End-joining activity in U2OS cells expressing mutated or WT Ku80. Error bars represent s.d., n=4

665 independent experiments. *p* values were calculated using unpaired two-tailed *t*-test: WT *vs*
666 E133M *p*=0.0004; WT *vs* I112R *p*=0.0052; WT *vs* I112R/E133M *p*=0.0002. **(f)** Distal end-
667 joining in U2OS cells containing mutated or WT Ku80. Error bars represent s.d., n=7
668 independent experiments. *p* values were calculated using unpaired two-tailed *t*-test: WT *vs*
669 E133M *p*=7.49 e-05; WT *vs* I112R *p*=2.21 e-06; WT *vs* I112R/E133M *p*=4.05 e-06. **(g)**
670 Survival of U2OS cells expressing WT or mutated Ku80. y axis is log scale. Error bars
671 represent s.d., n=7 to 10 independent experiments. *p* values were calculated using unpaired
672 two-tailed *t*-test: WT *vs* I112R p=1.47 e-06 ; WT *vs* E133M *p*=6.32 e-05 ; WT *vs*
673 I112R/E133M *p*=2.52 e-13 ; I112R *vs* E133M *p*=0.011. Significant *p*-values are indicated as
674 follows: **p*< 0.05, ***p* < 0.01, ****p* < 0.001. (**h)** Model for APLF and XLF KBMs function
675 during NHEJ.

Table 1 Data collection and refinement statistics

	Ku-pAPLF (PDB 6ERF)	Ku-pXLF (PDB 6ERH)	Ku-pXLFs (PDB 6ERG)
Data collection			
Space group	P_1	$P2_1$	$P2_1$
Cell dimensions :			
a, *b*, *c* (Å)	98.9, 140.8, 150.3	111.8, 118.9, 128.2	111.7, 114.3, 127.2
α, β, γ (°)	68.6, 80.8, 81.2	90.0, 93.1, 90.0	90.0, 93.1, 90.0
Resolution (Å)	49.5-3.0 (3.28-3.0)	49.01-2.8 (3.16-2.8)	50-2.9 (3.09-2.9)
Anisotropy resolution limits (Å)[§]	2.9, 3.9, 3.3	2.7, 4.4, 3.4	2.8, 3.8, 3.0
Resolution limit overall (Å)[§]	3.15	3.11	3.0
R_{merge}	0.056 (0.79)	0.164 (1.35)	0.171 (2.48)
R_{meas}	0.072 (0.93)	0.182 (1.47)	0.182 (2.56)
R_{pim}	0.051 (0.66)	0.094 (0.76)	0.068 (0.94)
I/σ (I)	11.8 (1.3)	9.1 (1.5)	9.7 (1.0)
$CC_{1/2}$	0.99 (0.60)	0.997 (0.60)	0.996 (0.51)
Completeness (spherical, %)[§]	66.5 (14.3)	51.3 (8.5)	72.9 (21.0)
Completeness (ellipsoidal, %)[§]	92.1 (70.1)	92.4 (69.6)	94.6 (68.5)
Redundancy	3.4 (3.5)	7.1 (6.9)	14.0 (14.2)
Refinement			
Resolution (Å)	49.47-3.01	49.38-2.8	48.76-2.9
No. reflections	90993	41644	51644
R_{work} / R_{free}	0.209/0.227	0.225/0.252	0.218/0.244
No. Atoms	35410	18810	18989
Protein	33225	16649	16821
DNA	2178	2118	2133
SO_4^{2-}	0	10	15
Water	7	33	20
B factors (Å^2)			
Protein	112	76	94
DNA	201	109	126
R.m.s. deviations			
Bond lengths (Å)	0.008	0.007	0.008
Bond angles (°)	0.96	0.95	0.95

*Values in parentheses are for highest-resolution shell. [§] Values from STARANISO, Global Phasing Ltd.

Table 2 : Interactions measured by microcalorimetry between Ku70/Ku80, A-KBM, X-KBM and XLF

	Protein in the measurement cell	Ligand in the syringe	K_d (µM)	ΔH (kcal.M^{-1})	Remarks
1	Ku_{FL}	pAPLF	0.033 ± 0.01	-13.3 ± 0.1	A-KBM (APLF 174-191)
2	Ku_{FL}	DNA 18bp	0.0041 ± 0.0007	+5.3 ± 0.2	DNA_{18bp} versus Ku
3	Ku_{FL}+DNA-18bp	pAPLF	0.023 ± 0.002	-16.0 ± 0.4	in presence of DNA_{18bp}
4	Ku_{CC}	pAPLF	0.020 ± 0.002	-18.4 ± 0.7	Ku without Cter domains
5	Ku_{FL} I112R	pAPLF	NI[(a)]	NI	Ku80 mutant on APLF site
6	Ku_{FL}	pXLF	4.4 ± 0.2	-2.8 ± 0.2	X-KBM (XLF 281-299)
7	Ku_{FL} +DNA-18bp	pXLF	2.4 ± 0.1	-8.1 ± 0.6	in presence of DNA_{18bp}
8	Ku_{CC}	pXLF	2.2 ± 0.9	-3.1 ± 1.2	Ku without Cter domains
9	Ku_{FL}	XLF	1.0 ± 0.1	-9.0 [(b)]	XLF versus Ku
10	Ku_{FL}+DNA-18bp	XLF	2.35 ± 0.1	-8.1 ± 0.6	XLF versus Ku/DNA_{18bp}
11	Ku_{FL}	pXLF(LW)	0.12 ± 0.03	-12.1 ± 2.0	X-KBM (L297W)
12	Ku_{FL}	pXLF(LE)	NI	NI	X-KBM (L297E)
13	Ku_{FL}+pAPLF	pXLF(LW)	NI	NI	L297W in presence of A-KBM

(a) NI means no interaction; (b) The enthalpy value was deduced from the first injection point in absence of lower plateau;
The thermograms and isotherms of titration of the experiments corresponding to lines 1, 6 and 11 are presented in Supplementary Figure 2e-g.
Interactions in lines 1, 4, 6, 8, 9, 11 were measured in triplicate, and the mean value with standard deviation is reported. Interactions in lines 2, 3, 4, 6, 10 were measured in duplicate, and the mean value with variation between min and max values is reported.

ONLINE METHODS

DNA preparation

The 500 bp linear dsDNA molecules were amplified from the 3516-4016 region of pBR322 plasmid with biotinylated primers (5'-bGGATCTCAACAGCGGTAA-3' and 5' bCTTTATCCGCCTCCATCC-3'). DNA fragments were purified on a MiniQ anion exchange column with a chromatography SMART system (GE Healthcare), ethanol precipitated and resuspended in a 10 mM Tris-HCl, pH 7.5, 1 mM EDTA buffer.

Oligonucleotides for ITC and EMSA

CN1 34bp : CGCGCCCAGCTTTCCCAGCTAATAAACTAAAAAC

CN2 21bp : GTTTTTAGTTTATTGGGCGCG

CN3 18bp up : GTTATCCGAGCGTGAGAC

CN4 18bp down : GTCTCACGCTCGGATAAC

NLB48 : TAG TCG TAA GCT GAT ATG GCT GAT TAG TCG GAA GCA TCG AAC GCT GAT

MM 50bp up : FAM-TAAATGCCAATGCTGCTGATACGTACTCGGACTGATTCGGAACTGTAACG

MM 50bp do : CGTTACAGTTCCGAATCAGTCCGAGTACGTATCAGCAGCATTGGCATTTA

Peptides and Proteins:

The synthetic peptides containing the KBM and XLM motifs were purchased from Genecust at 95% purity, and the concentrations of the stock peptide solutions were determined by amino acid composition. The oligonucleotides used for ITC and crystallization were synthesized by Sigma-Aldrich and Eurogentec.

The full length Ku70(1-609)/Ku80(1-732) heterodimer and a truncated version of the heterodimer deleted Ku70(1-544)/Ku80(1-551) were cloned in the Multibac vectors with a 10-His tag and a TEV site on the Ku80 N-terminus [53]. Each plasmid was integrated in a Yellow Green Protein (YFP) containing bacmid by transformation in EMBACY *E.coli* stain (kind gift from Imre Berger, Bristol University). The resulting recombinant bacmids were used to transfect Sf21 insect cells giving the V0 virus generation. After amplification, stocks of viruses were titrated by the dilution limit method using YFP as marker for infected cells and Mac Grady table. Production was initiated in Sf21 cells culture by infection with baculovirus at MOI of $5x10^{-3}$. Insect cells were collected 5-6 days after the infection (3-4 days

after the proliferation arrest). Cells were sonicated and the supernatant was incubated with Benzonase (300 units for 30 min at 4°C). The Ku heterodimer was purified on a NiNTA-Agarose affinity column (Protino, Macherey Nagel) with a 1M NaCl wash step to remove DNA excess. The eluted Ku was then bound onto an anion exchange column (Resource Q, GE Healthcare) equilibrate with buffer Q (20 mM Tris pH 8.0, 50 mM NaCl, 50 mM KCl, 10 mM β-mercaptoethanol). Final yield of the Ku heterodimer was typically 35 mg of purified heterodimer by liter of culture. The full length 10-His tagged XLF protein was produced in insect cells with a similar protocols with a yield of 50mg of purified protein by L of culture. A truncated version of XLF(1-224) was also produced in *E. coli* .

Crystallization of the Ku70/Ku80/hDNA complexes with A-KBM and X-KBM peptides

The DNA used in this study is the hairpin DNA previously used by Walker et al [3]. It was obtained using HPLC-purified oligonucleotide of 34 and 21 nucleotides (see oligonucleotides above). The oligonucleotides were annealed and added in 1.1-fold molar excess to Ku heterodimer. The peptides containing the A-KBM motif (18mer, 174-192), the long X-KBM motif (19mer, 281-299) or the short X-KBM motif (13mer 287-299) were added respectively with a 1.1, 2 and 2 fold excess. Crystallization screenings on the Ku_{CC}-hDNA-peptides were performed on the HTX platform (EMBL, Grenoble) with an automatic visualization at 4°C. The crystals of Ku_{cc}-hDNA-pAPLF were reproduced and optimized in the laboratory at 20 °C using the sitting drop method by mixing 1.5µL of the 20 mg/mL Ku-DNA-peptides complexes with 1.5 µL of the solution containing 13% polyethylene glycol (PEG) 3350, 150 mM $NaNO_3$, and 100 mM Bis-Tris-Propan (pH 6.5). The crystals (100x150x1000µm) grew in 5-6 hours and were frozen in a solution of the mother liquor with 20% glycerol. The Ku_{cc}-hDNA-pXLF and Ku_{cc}-DNA-pXLFs complexes were crystallized at 20 °C by mixing 1.5µL of the 7 mg/mL complex solution with 1.5 µL of a solution containing 18% polyethylene glycol (PEG) 3350, 150 mM Na_2SO_4, and 100 mM Bis-Tris-Propane (pH 8,5). The crystals (100x200x50µm) grew in 5-6 days and were frozen with 20% glycerol.

Determination of the crystal structures

Diffraction data were collected at the Proxima 1 and Proxima 2 beamlines at the *synchrotron* SOLEIL. The datasets were indexed and integrated using the XDS package [54], the XDSME package (XDS Made Easier, https://github.com/legrandp/xdsme) and the CCP4 suite [55]. The crystals present a highly anisotropic diffraction (between 2.85Å and 4.25Å resolution according to the axes). The anisotropy of Kucc-hDNA-pAPLF crystals was treated with the

754 STARANISO program (http://staraniso.globalphasing.org/). The software performs an
755 anisotropic cut-off of merged intensity data, a Bayesian estimation of the structure
756 amplitudes, and applies an anisotropic correction to the data. The structure of the Ku70/80-
757 hDNA-pAPLF was determined by molecular replacement with the program MOLREP using
758 the structure of Ku70/80 (pdb 1JEY) without the DNA coordinates [3]. Four molecules of Ku
759 were consecutively positioned. Electron density for the hDNA was clearly visible in the
760 position previously reported by Walker. Refinement was performed using BUSTER [56] and
761 PHENIX [57]. The models were built with Coot [58]. After DNA building, an electron density was
762 visible on the Ku80 vWA near the Ku80 amino acids identified by Grundy et al by
763 mutagenesis. The final statistics are presented below. In the final model, the following regions
764 of Ku70/Ku80 are not visible: Ku70 1-33, 535-544 and Ku80 1-5, 170-181, 190-191, 543-
765 551.. The quality of the model was assessed using Molprobity [59].
766 The crystal structures of the Ku70/80-hDNA complexed with the long and short pXLF were
767 solved by molecular replacement. Firstly, the coordinates of Ku70/80 and the hairpin DNA
768 present in pdb 1JEY were used as model. We positioned two molecules in the asymmetric
769 unit with clear electron density except on the vWA region of Ku80 (region aa 6 to 242). We
770 then performed the molecular replacement with the same coordinates deleted of the Ku80
771 vWA region. The electron density for the secondary structure elements of the Ku80 vWA was
772 clearly visible though at a different position than in 1JEY. A second molecular replacement
773 step was performed to position the vWA domain of the two Ku80 molecules in the
774 asymmetric unit. The structure of the Ku70/80-DNA-short pXLF was solved in a similar
775 manner. An electron density was visible in an internal position of Ku80 vWA that could be
776 attributed to pXLF. The final statistics are presented in Table1. In the final model with the
777 long pXLF, the following regions of Ku70/Ku80 are not visible (Ku70 1-34, 535-554 and
778 Ku80 543-544). In the final model with the short pXLF, the following regions of Ku70/Ku80
779 are not visible (Ku70 1-34; 535-554 and Ku80 171-194, 300-301, 542-544).
780 An additional electron density was observed in the long and short pXLF complex structures
781 located close to the extreme N-terminus of Ku80 and to the hairpin DNA. This electron
782 density was successfully modeled with the first missing residues of Ku80, the TEV site
783 sequence preceding (ENLYFQG) and seven histidines from the 10-His tag. To evaluate the
784 influence of the tag present on the N-terminus of Ku80 on the Ku-XLF interaction, we
785 prepared a digested form of Ku with the TEV protease (Ku^{TEV}) and measured by ITC its
786 interaction with the X-KBM. The ITC shows that thermodynamic parameters of the Ku^{TEV} are

similar to the Ku and that the tag does not significatively influence the binding of the XLF motif.

Small-angle Xray scattering: Several data of Ku_{cc}-hDNA complex with a protein-DNA ratio (1:1.2) were collected alone or in presence of pXLF or pAPLF peptides. Data were collected on the SWING beamline (SOLEIL synchrotron) at a 1.8m sample-detector distance. The complexes were prepared at 1.0, 3.0 and 5mg/mL and spun for 10 minutes at 13000 rpm prior to SAXS analysis to eliminate aggregates. Volumes of 40µL of each sample and buffer (20 mM Tris pH 8.0, 150mM NaCl, 5mM β-mercaptoethanol) were injected into the SAXS capillary cell and collected continuously, with a frame duration of 0.5 s and a dead time between frames of 0.5 s. Data reduction to absolute units, frame averaging and subtraction were done using FOXTROT [60], a dedicated home-made application. All subsequent data processing and analysis steps were carried out with PRIMUS and other programs of the ATSAS suite [61]. The program GNOM [62] was used to compute the pair-distance distribution functions, *P(r)*.

Isothermal titration Calorimetry (ITC)

Interactions between Ku70/80 wild-type and Ku70/80cc and the different peptides containing the KBM and XLM motifs were determined by isothermal titration calorimetry (ITC) using a VP-ITC calorimeter (Malvern). Prior to measurements, all solutions were degassed under vacuum. The reaction cell of the ITC (volume 1.8 mL) was loaded with Ku heterodimers alone or complexed with DNA or peptides for competition experiments. Proteins were extensively dialyzed against buffer I (20 mM Tris, pH 8.0, 150 mM NaCl, and 5 mM β-mercaptoethanol). Peptides and DNA were prepared at high concentrations. The syringe (290 µL) was filled with the different peptides at concentration between 20 µM to 200 µM. The Ku heterodimer present in the cell was titrated by automatic injections of 6-10µL of the different peptides. Enthalpy ΔH (in $kcal.mol^{-1}$), stoichiometry of the reaction N, and association constant Ka (in M^{-1}) were obtained by nonlinear least-squares fitting of the experimental data using the single set of independent binding sites model of the Origin software provided with the instrument. The free energy of binding (ΔG) and the entropy (ΔS) were determined using the classical thermodynamic formula, $\Delta G = - RT \ln(Ka)$ and $\Delta G = \Delta H - T\Delta S$. All binding

experiments were performed in duplicate or triplicate at 25°C. Control experiments were performed with peptides injected into the buffer to evaluate the heat of the dilution.

EMSA:

Binding reactions (10 µL) were performed by incubating the annealed oligonucleotides (oligonucleotides used in this study are listed in Table Sxx and indicated in the figure legends) at a final concentration of 25 nM, with the indicated final concentrations of proteins in 75 mM KCl, 10 mM Tris (pH 7.5), 0.5 mM EDTA, 0.5 mM DTT, 0.5 mg/mL acetylated-BSA, and 5% glycerol. Reactions were incubated at room temperature for 1 hr and fractionated by 6% PAGE (29%/1% [w/v] Acrylamide:Bis-acrylamide) in 0.53 standard Tris-borate-EDTA (TBE) buffer at 80 V for 45 min to 1 hr. After electrophoresis, DNA was visualized using a ChemiDoc MP imaging system (Bio-Rad), either by direct detection of the fluorescently labeled DNA (FAM) or after staining with 0.2 mg/mL EtBr. Data were processed and quantified with the Image Lab software version 5.2.1 (Bio-Rad).

switchSENSE measurements :

All switchSENSE measurements were carried out on a DRX 2400 instrument, using a multi-purpose 48bp chip (both Dynamic Biosensors GmbH; Planegg, Germany). The sample and running buffer was Tris 10mM pH 7.4, 140mM NaCl, 0.05% Tween20, 50µM EDTA, 50µM EGTA. In all kinetics experiments, complementary DNA to the strand immobilized on the chip was first hybridized on the measurement electrodes. On top of the 48bp complementary to the chip, this DNA carried a 32bp-overhang hybridized with its 32bp complementary strand. Second, the Ku70/80 protein was associated at 100nM for 3min (reaching saturation) to the immobilized dsDNA. Finally, the association and dissociation of the XLF protein was measured using triplicates of each concentration, at a flow rate of 2mL/min. For each mutant, the surface was not regenerated in between concentrations – Ku does not dissociate in the timescale of the XLF measurement, and XLF fully dissociates for each concentration. The electrodes were only regenerated between the measurements of different mutants of XLF. Kinetics values were determined using Origin software.

Cell lines and cell culture

U2OS human osteosarcoma cells and immortalized BuS cells (derived from an XLF-deficient patient, gift from Jean-Pierre de Villartay, Institut Imagine, Paris, France) were grown in DMEM and RPMI, respectively. Media were supplemented with 10% fetal calf

serum (Eurobio), 125 U/ml penicillin and 125 µg/ml streptomycin. Cells were maintained at 37°C in a 5% CO2 humidified incubator. Cell lines were tested negative for mycoplasma by PCR. All culture media and antibiotics were from Invitrogen. When necessary (conditional expression of shRNA against Ku80), doxycyclin (Sigma-Aldrich) was added to the medium at a 4 µg/ml final concentration.

Expression vectors

See Supplementary Data Set 1

Cell transfection and transduction

Production of lentiviral particles in HEK-293T cells and transduction of U2OS and BuS cells were performed as previously described [31]. Transduced cells were used as populations without clonal selection, except when indicated otherwise.

Plasmid recircularization assay

U2OS cell populations expressing wild-type or mutated Ku80 protein were seeded to near confluence in 6-well plates and incubated overnight at 37°C. Cells were then transfected with 1 µg BamHI-linearized pEGFP-N1 plasmid (Clontech) and 1 µg pmCherry-C1-3NLS circular plasmid as a transfection control (gift from Dyche Mullins (Addgene #58476), [63]). Cells were split 24 h later, incubated at 37°C for two additional days and analyzed by flow cytometry on a Fortessa X-20 (BD Biosciences). For each cell population, the integrated GFP fluorescence signal was normalized to mCherry signal. End-joining activity was set to 100% for Ku80-WT expressing cells. Results were plotted as the mean values of four independent experiments ±s.d.

Distal End-Joining assay

U2OS-EJ5 cells (a kind gift from Jeremy Stark, City of Hope, Duarte, USA) containing one integrated copy of a GFP reporter cassette which allows to measure rejoining of two tandem I-SceI cut sites separated by a ~1.8-kb insert, were modified as follows. The cells were first transduced with lentiviruses produced from pLV-tTR-KRAB and pLV3-Tet-RFP-ISceI-GRLBD to allow inducible expression and nuclear translocation of the I-SceI yeast meganuclease. The resulting cells were then transduced with lentiviruses prepared from pLVTHM2-shKu80. A positive clone enabling doxycyclin-dependent conditional knockdown of Ku80 expression and subsequent cell death was isolated. These cells were further

transduced with lentiviruses produced from pLV3-HA-Ku80-shR-(WT or mutants) plasmids to replace, in the presence of doxycyclin, endogenous Ku80 expression by expression of the various Ku80 constructs described in the study. To perform Distal End-Joining assay, the different U2OS-EJ5 modified cell populations were seeded onto 6-well plates and incubated at 37°C for 24 h. Dexamethasone (Sigma-Aldrich) was then added to a final concentration of 250 nM. Cells were washed 24 h later, further incubated at 37°C for two to three days and analyzed by flow cytometry on a Fortessa X-20 analyzer (BD Biosciences). The fraction of GFP-positive cells was measured and normalized to 100% for Ku80-WT expressing cells. Results were plotted as the mean values of seven independent experiments ±s.d.

Ionizing irradiation and cell survival analysis

Three to six thousand cells per well were seeded in 6-well plates. Plated cells were exposed 24 h later to various doses of X-ray using a Faxitron RX-650 device (130 kV, 5 mA, dose rate 0.5 $Gy.min^{-1}$). Six to seven days later, cells were washed with PBS, stained 10 min with crystal violet (0.1% aqueous solution). Stained cells were extensively washed with water and plates were air dried. Staining was dissolved with 10% acetic acid solution and absorption was measured at 570 nm (Ultrospec-3000 spectrophotometer, Pharmacia Biotech). Results were plotted as mean values of 5-10 independent experiments ±s.d. using Microsoft Excel software.

Live-cell microscopy and micro-irradiation

U2OS or BuS cells were seeded in 35-mm glass-bottom culture dishes (MatTek) two days prior laser irradiation. Experiments were carried out with a Zeiss LSM-710 confocal laser scanning microscope equipped with a coherent chameleon Vision-II tunable laser (690-1080 nm), a 40X/1.3 oil immersion objective and a heated environmental chamber set at 37°C in 5% CO2 atmosphere. ECFP was excited using biphotonic laser at 800 nm (1.5% of maximum power). Confocal image series were recorded with a frame size of 512×512 pixels. Nuclei micro-irradiation was carried out at 800 nm at 20% of maximum power (mean max power was 3070 mW) in rectangle of 15 μm^2 area during 50 µs pixel dwell time. Before and after micro-irradiation, confocal image series of one mid z-section were recorded at 1.94 s time interval (typically 9 pre-irradiation and 40-45 post-irradiation frames). For evaluation of the recruitment kinetics, fluorescence intensities of the irradiated region were corrected for total nuclear loss of fluorescence over the time course and normalized to the pre-irradiation value. Data from micro-irradiation of individual cells obtained in several independent

experiments performed on different days were averaged, analyzed and displayed using PRISM software. *p* values at last time point were calculated using unpaired Student's t-test.

Protein extraction and immunoblotting

Sub-confluent cells from 60-mm culture dishes were harvested and washed with PBS. Pellets were resuspended in 100 µl of lysis buffer (50 mM HEPES.KOH pH 7.5, 450 mM NaCl, 1% Tritin-X100, 1 mM EDTA, 1 mM DTT, protease-phosphatase Halt Inhibitor cocktail (Pierce, Thermo Scientific)) and processed by four freeze/thaw cycles. After centrifugation at 14000 g for 10 min, protein concentration was measured in the supernatant with the Bradford assay (Bio-Rad). Proteins from 50 µg of cell extracts were separated in 4-15% Mini-Protean TGX precast polyacrylamide gels (Bio-Rad) and transferred to PVDF membrane (Millipore). Immunoblotting analysis was performed with the following antibodies: anti-Ku70 monoclonal antibody (clone N3H10 from NeoMarkers), anti-Ku80 monoclonal antibody (clone 111 from Thermo Fisher Scientific), anti-DNA-PKcs monoclonal antibody (clone 18.2 from Abcam), anti-XLF polyclonal antibody (Bethyl Laboratories), anti-APLF polyclonal antibody (SK3595, kind gift from K.W. Caldecott, University of Sussex, Brighton, UK, see [25]), anti-β-Actin monoclonal antibody (clone AC-15 from Ambion).

Cell culture and preparation for super-resolution imaging

BuS cells were grown in RPMI medium with 10% FBS and 100 U/mL Penicillin-Streptomysin. For super-resolution imaging, cells were cultured on glass coverslips for 24 hours, followed by serum starvation for 48 hours. The cells were then released into full medium for 4 hours so that most of the cells were in G1 phase.

The synchronized cells were then washed twice with PBS, and permeabilized with 0.5% Triton X-100 in CSK buffer (10 mM Hepes, 200 mM Sucrose, 100 mM NaCl, and 3 mM $MgCl_2$, pH=7.4) for 10 minutes [64]. Cells were then fixed with paraformaldehyde (4%) for 20 mins, and blocked in block solution (2% glycine, 2% BSA, 0.2% gelatin, and 50 mM NH_4Cl in PBS) overnight at 4°C.

Fixed cells were then immunostained with validated monoclonal antibodies: XLF was stained with XLF-antibody (3D6, NBP2-03275, NOVUS) for 1 hour at room temperature, followed by Alexa Fluor 647 conjugated goat-anti-mouse 2nd antibody staining (ab 150115, abcam) for 30 minutes at room temperature. Cells were then stained with Alexa Fluor conjugated anti-Ku80 antibody (EPR3467, ab202659, abcam) for 1 hour at room temperature.

Cells were then mounted onto microscope glass slide, and imaged with freshly mixed imaging buffer (1 mg/mL glucose oxidase, 0.02 mg/mL catalase, 10% glucose, and 100 mM cycteanube (MEA)).

Microscope and Single-Molecule Localization imaging

Super-resolution imaging was performed on a custom-built optical imaging platform based on a Leica DMI 300 inverse microscope, equipped with a 488 nm (OBIS, Coherent) and a 639 nm laser line (MRL-FN-639-800, CNI). Laser lines were reflected into an HCX PL APO 63X NA=1.47 OIL CORR TIRF Objective (Zeiss) by a penta-edged dichroic beam splitter (FF408/504/581/667/762-Di01-22x29), and the emitted fluorescence was further extended by a 2X lens tube (Diagnostic Instruments), filtered by single-band filters (Semrock FF01-531/40 and FF01-676/37 for Alexa Fluor 488 and Alexa Fluor 647, respectively), and collected onto a sCMOS camera (Prim95B, Photometrics). A 405 nm Laser line (MDL-III-405-150, CNI) was also equipped to reactivate Alexa Fluor 647 fluorophores.

For super-resolution imaging, the 488 and 639 laser lines were adjusted to ~ 1.0 and 1.5 kW/cm2, and a Highly Inclined and Laminated Optical sheet (HILO) illumination mode for sample excitation. Alexa Fluor 488 and Alexa Fluor 647 were sequentially exited and their emitted fluorescence was also sequentially collected by switching the single-band filters in a filter wheel. The emitted photons were collected onto a sCMOS camera (Photometrics Prime 95B), and a minimum of 2000 frames at 33 Hz were recorded for each image stack.

Reconstruction from Single-Molecule Localization image to super-resolution image

Each image of the image stack was first of all box-filtered with the box size of 4 times of the FWHM of a 2D gaussian point spread function (PSF). Considering the patterned noise for sCMOS camera construction, each pixel was weighted by the inverse of its noise variance during filtering. The low-pass filtered image was then extracted as the background from the raw image. The local maximums of the image were then recognized and segmented into single PSFs for 2D gaussian fit.

2D gaussian fit of each individual PSF was performed by GPU using the Maximum Likelihood Estimation (MLE) algorithm. Briefly, the likelihood function of each pixel was constructed by convolving the Poisson distribution of the shot noise governed by the photons emitted from fluorophores nearby, and the gaussian distribution of the readout noise of the camera itself [65]. The offsets, variance, and analog-to-digital conversion factor of each pixel of the camera was calibrated beforehand. The position, amplitude, sigma, and background of

each individual 2D gaussian PSF were addressed by maximizing the likelihood function of each pixel given its readout digital value. The fitting accuracy was estimated by Cramér-Rao lower bound (CRLB) and the accuracy of Alexa Fluor 488 and Alexa Fluor 647 in this work are ~ 17 and 13 nm, respectively.

Alignment of images of different colors

Mapping of the two colors was performed using a polynomial mapping algorithm. Briefly, a spatially separated and broad-spectrum fluorescent bead (TetraSpec, ThermoFisher) slide was imaged on both color channels. Mass centers of each same bead but in different channels were recorded pairwise. The coefficient of each term in a 2nd order polynomial function was optimized by training the polynomial regression using all the recorded bead's centers. The optimized polynomial function was then used for two color channels alignment. We note that choosing the proper order of polynomial function for optimization depends on the number of training beads, and higher order but not enough trainees would lead to overfit.

Pair-Correlation analysis

Coordinates localized within ~2.5 times of the averaged localization uncertainty, and from consecutive frames were considered as artificial blinking and grouped as one coordinate. This coordinate was calculated by taking the 1/var weighted average of all the coordinates within the group, where var is the localization uncertainty of each coordinate. The grouped coordinates were then rendered onto a pixelized image of 5 nm/pixel, and the pair-correlation was performed on this image by series 2D Fourier and inverse Fourier transfers [66].

The correlation was then fitted into two correlation terms: the correlation among coordinates within localization uncertainty, and that among the coordinates that form a cluster/molecular assemble/filament. Considering the size of XLF 'clusters' is not randomly distributed, we fitted the second term into a normal distribution and interpret the fitted sigma as the apparent radius of the averaged XLF 'cluster' radius (Figure XC) across the image.

Data availability

Crystal structures are deposited at the pdb with the following codes Ku-DNA-pAPLF (6ERF), Ku-DNA-pXLF (6ERH) and Ku-DNA-pXLFshort (6ERG)

Source data for figures 3, 4 and 5 are available with the paper online

Other data that support the findings of this study are available from the corresponding author upon reasonable request.

METHODS-ONLY-REFERENCES

53. Bieniossek, C., Imasaki, T., Takagi, Y. & Berger, I. MultiBac: expanding the research toolbox for multiprotein complexes. *Trends Biochem Sci* **37**, 49-57 (2012).
54. Kabsch, W. XDS. *Acta Crystallogr D Biol Crystallogr* **66**, 125-32 (2010).
55. Winn, M.D. et al. Overview of the CCP4 suite and current developments. *Acta Crystallogr D Biol Crystallogr* **67**, 235-42 (2011).
56. Smart, O.S. et al. Exploiting structure similarity in refinement: automated NCS and target-structure restraints in BUSTER. *Acta Crystallogr D Biol Crystallogr* **68**, 368-80 (2012).
57. Afonine, P.V. et al. Towards automated crystallographic structure refinement with phenix.refine. *Acta Crystallogr D Biol Crystallogr* **68**, 352-67 (2012).
58. Emsley, P., Lohkamp, B., Scott, W.G. & Cowtan, K. Features and development of Coot. *Acta Crystallogr D Biol Crystallogr* **66**, 486-501 (2010).
59. Chen, V.B. et al. MolProbity: all-atom structure validation for macromolecular crystallography. *Acta Crystallogr D Biol Crystallogr* **66**, 12-21 (2010).
60. Perez, J. & Nishino, Y. Advances in X-ray scattering: from solution SAXS to achievements with coherent beams. *Curr Opin Struct Biol* **22**, 670-8 (2012).
61. Petoukhov, M.V. et al. New developments in the ATSAS program package for small-angle scattering data analysis. *J Appl Crystallogr* **45**, 342-350 (2012).
62. Svergun, D.I. Small-angle X-ray and neutron scattering as a tool for structural systems biology. *Biol Chem* **391**, 737-43 (2010).
63. Belin, B.J., Lee, T. & Mullins, R.D. DNA damage induces nuclear actin filament assembly by Formin -2 and Spire-(1/2) that promotes efficient DNA repair. *Elife* **4**, e07735 (2015).
64. Britton, S., Coates, J. & Jackson, S.P. A new method for high-resolution imaging of Ku foci to decipher mechanisms of DNA double-strand break repair. *J Cell Biol* **202**, 579-95 (2013).
65. Huang, F. et al. Video-rate nanoscopy using sCMOS camera-specific single-molecule localization algorithms. *Nat Methods* **10**, 653-8 (2013).
66. Veatch, S.L. et al. Correlation functions quantify super-resolution images and estimate apparent clustering due to over-counting. *PLoS ONE* **7**, e31457 (2012).

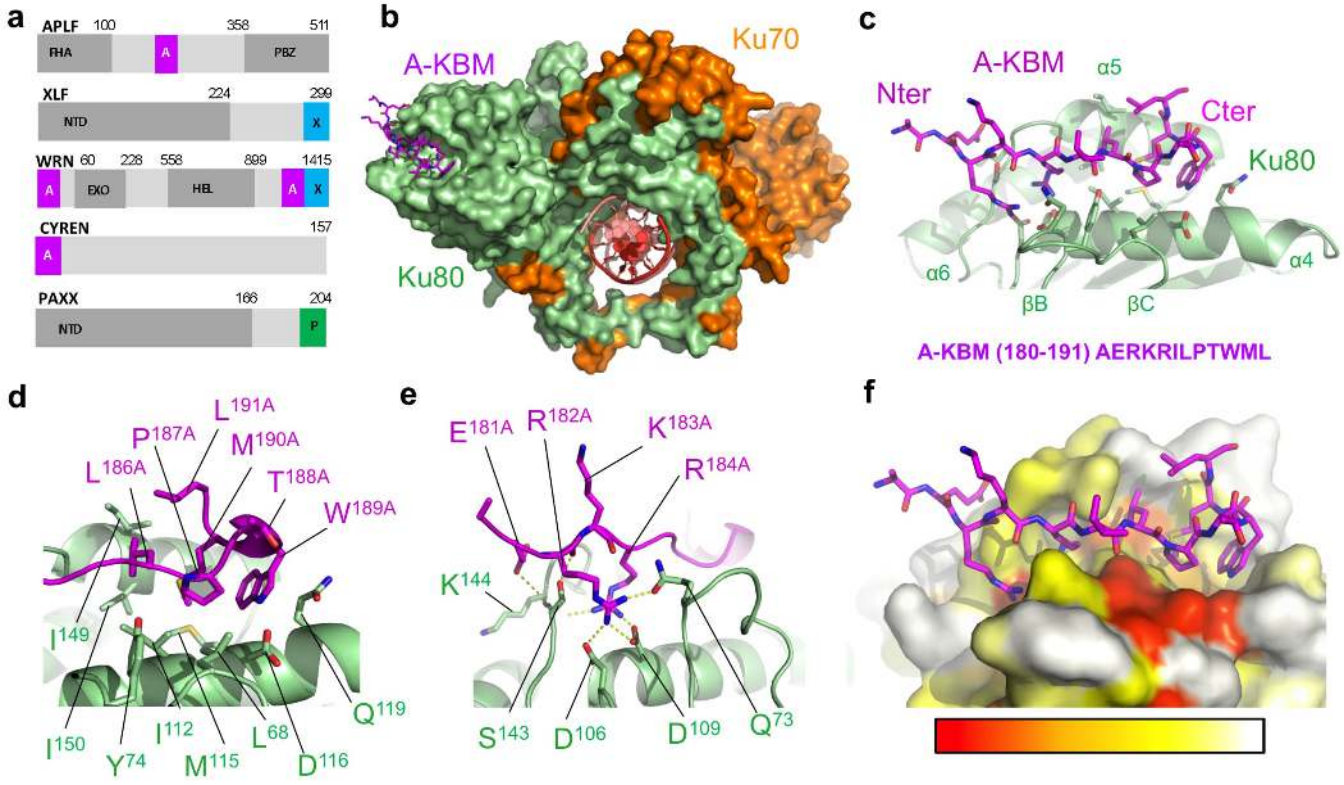
a
APLF
100
358
511
FHA
A
PBZ
XLF
224
299
NTD
X
WRN
60
228
558
899
1415
A
EXO
HEL
A
X
CYREN
157
A
PAXX
166
204
NTD
P
b
A-KBM
Ku70
Ku80
c
A-KBM
α5
Nter
Cter
Ku80
α6
α4
βB
βC
A-KBM (180-191) AERKRILPTWML
d
L191A
P187A
M190A
L186A
T188A
W189A
I149
I150
Y74
I112
M115
L68
D116
Q119
e
E181A
R182A
K183A
R184A
K144
S143
D106
D109
Q73
f

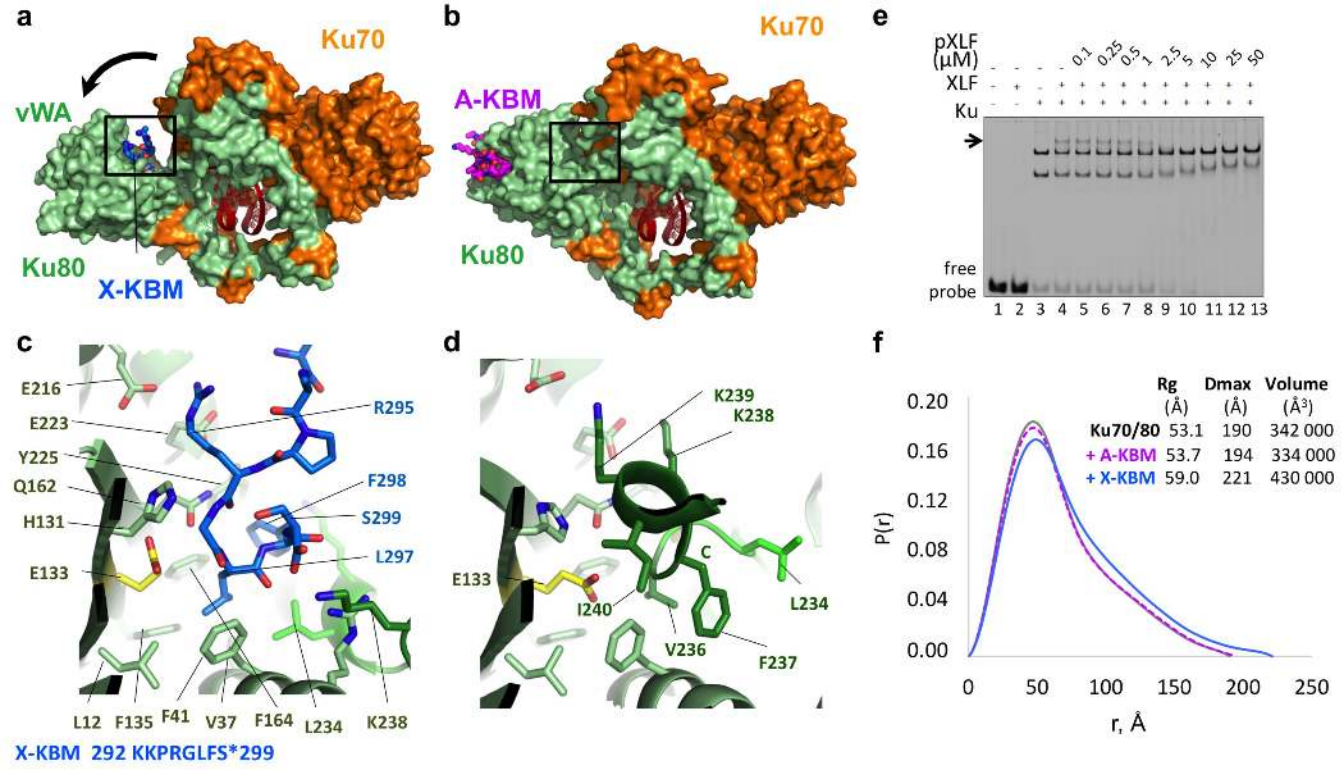
a
Ku70
vWA
Ku80
X-KBM
b
Ku70
A-KBM
Ku80
e
pXLF (μM)
0.1
0.25
0.5
1
2.5
5
10
25
50
XLF
Ku
free probe
1 2 3 4 5 6 7 8 9 10 11 12 13
c
E216
E223
Y225
Q162
H131
E133
R295
F298
S299
L297
L12
F135
F41
V37
F164
L234
K238
X-KBM 292 KKPRGLFS*299
d
K239
K238
E133
I240
C
L234
V236
F237
f
Rg (Å)
Dmax (Å)
Volume (Å3)
Ku70/80 53.1 190 342 000
+ A-KBM 53.7 194 334 000
+ X-KBM 59.0 221 430 000
P(r)
0.20
0.16
0.12
0.08
0.04
0.00
0
50
100
150
200
250
r, Å

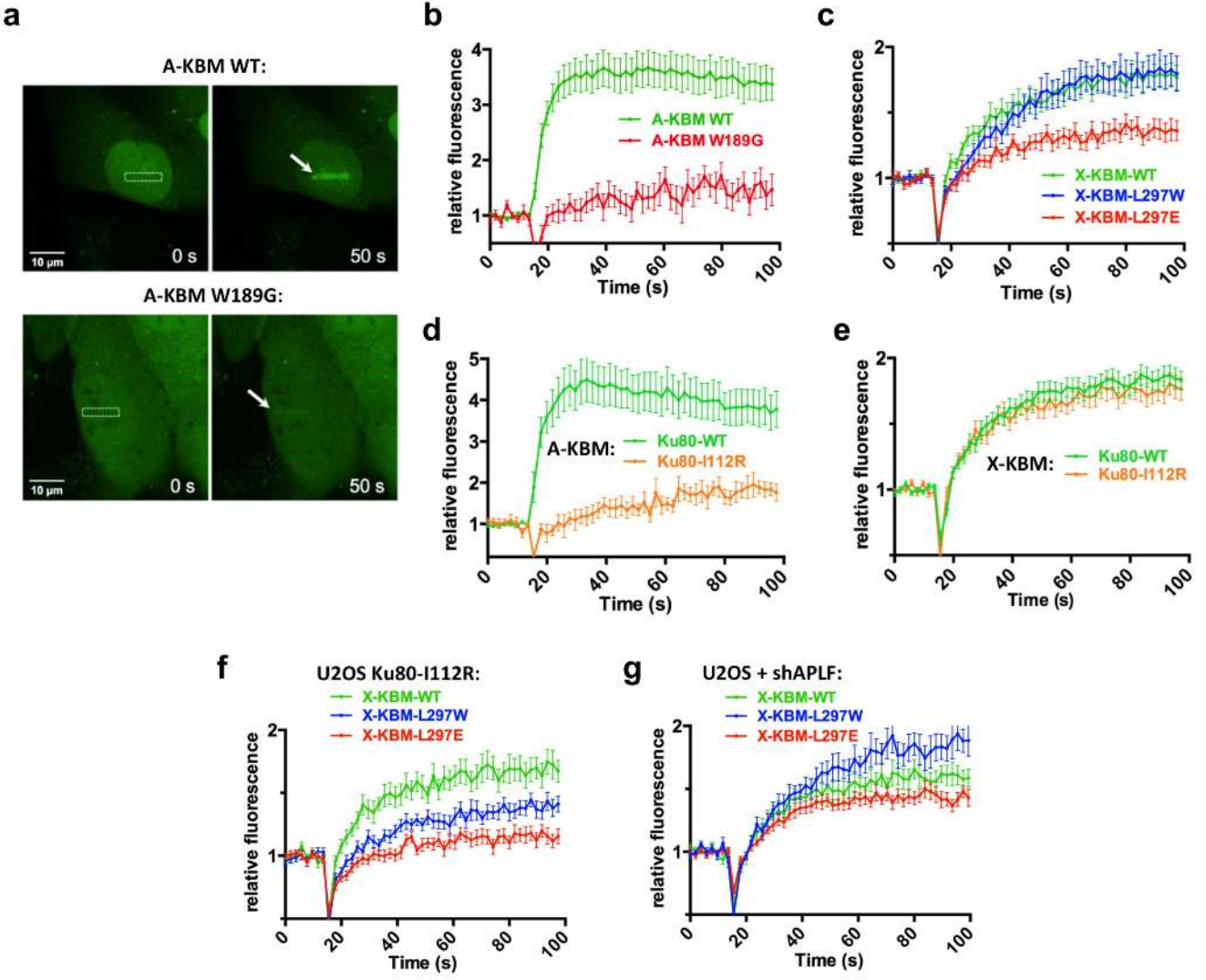
a
A-KBM WT:
10 μm
0 s
50 s
A-KBM W189G:
10 μm
0 s
50 s
b
relative fluorescence
A-KBM WT
A-KBM W189G
Time (s)
c
relative fluorescence
X-KBM-WT
X-KBM-L297W
X-KBM-L297E
Time (s)
d
relative fluorescence
A-KBM:
Ku80-WT
Ku80-I112R
Time (s)
e
relative fluorescence
X-KBM:
Ku80-WT
Ku80-I112R
Time (s)
f
U2OS Ku80-I112R:
X-KBM-WT
X-KBM-L297W
X-KBM-L297E
relative fluorescence
Time (s)
g
U2OS + shAPLF:
X-KBM-WT
X-KBM-L297W
X-KBM-L297E
relative fluorescence
Time (s)

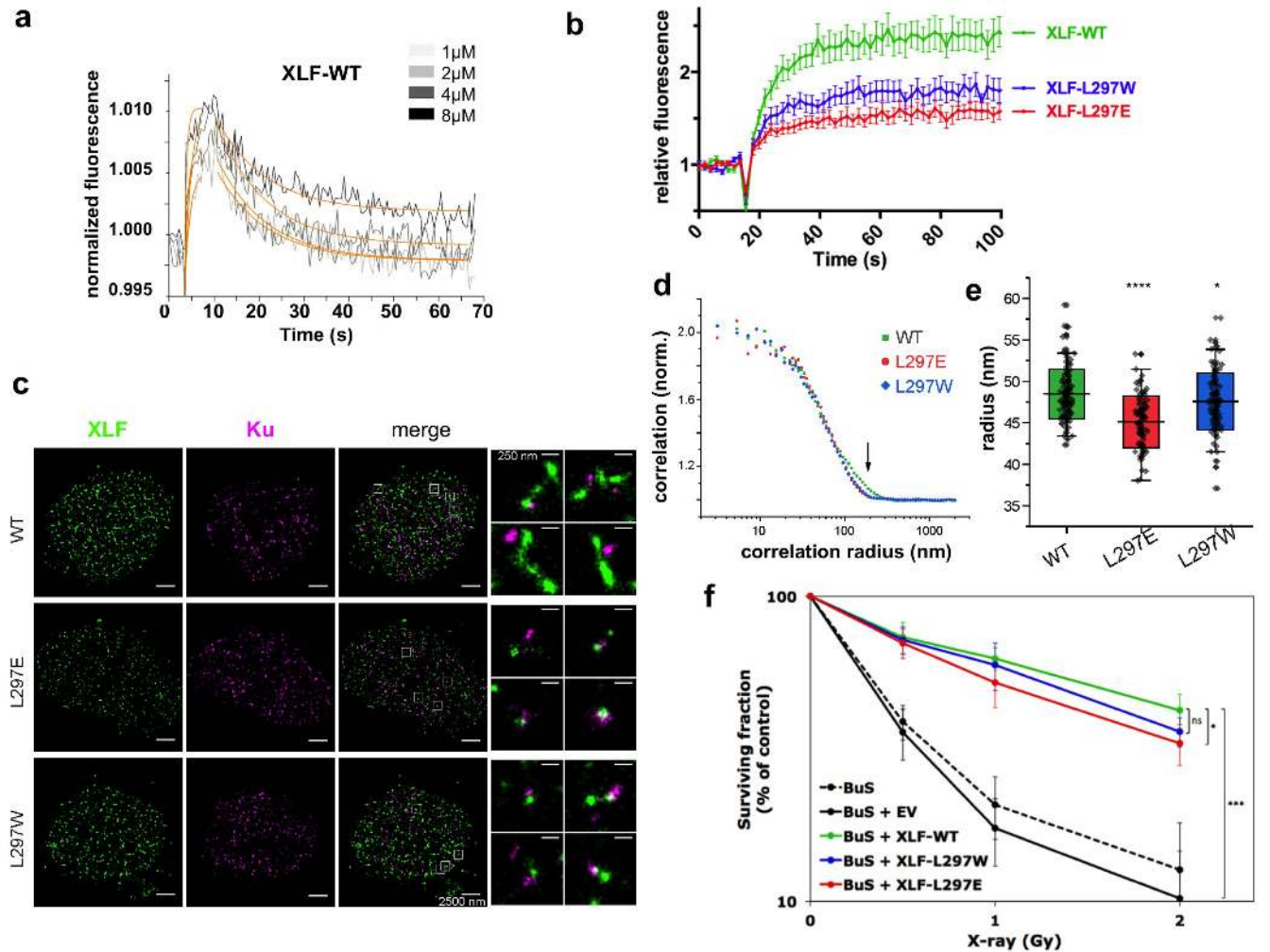
a
XLF-WT
1μM
2μM
4μM
8μM
normalized fluorescence
1.010
1.005
1.000
0.995
0
10
20
30
40
50
60
70
Time (s)
b
relative fluorescence
2
1
0
20
40
60
80
100
Time (s)
XLF-WT
XLF-L297W
XLF-L297E
c
XLF
Ku
merge
WT
L297E
L297W
250 nm
2500 nm
d
correlation (norm.)
2.0
1.6
1.2
10
100
1000
correlation radius (nm)
WT
L297E
L297W
e
radius (nm)
60
55
50
45
40
35
****
*
WT
L297E
L297W
f
Surviving fraction
(% of control)
100
10
0
1
2
X-ray (Gy)
ns
*
***
BuS
BuS + EV
BuS + XLF-WT
BuS + XLF-L297W
BuS + XLF-L297E

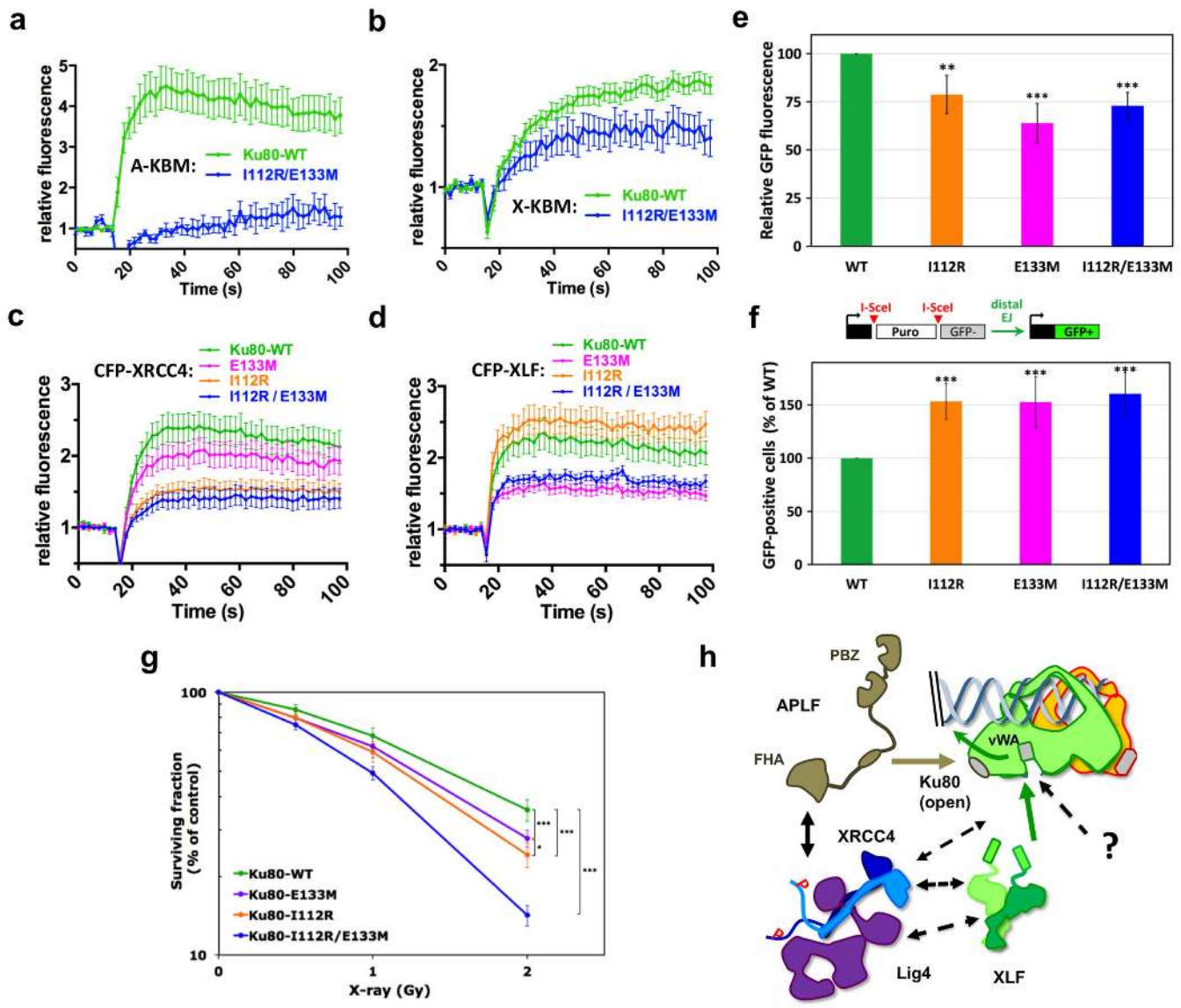
a
relative fluorescence
A-KBM:
Ku80-WT
I112R/E133M
Time (s)
b
relative fluorescence
X-KBM:
Ku80-WT
I112R/E133M
Time (s)
e
Relative GFP fluorescence
WT
I112R
E133M
I112R/E133M
c
CFP-XRCC4:
Ku80-WT
E133M
I112R
I112R / E133M
relative fluorescence
Time (s)
d
CFP-XLF:
Ku80-WT
E133M
I112R
I112R / E133M
relative fluorescence
Time (s)
f
I-SceI
I-SceI
Puro
GFP-
distal EJ
GFP+
GFP-positive cells (% of WT)
WT
I112R
E133M
I112R/E133M
g
Surviving fraction (% of control)
Ku80-WT
Ku80-E133M
Ku80-I112R
Ku80-I112R/E133M
X-ray (Gy)
h
PBZ
APLF
FHA
vWA
Ku80 (open)
XRCC4
?
Lig4
XLF

Sup Figure 1

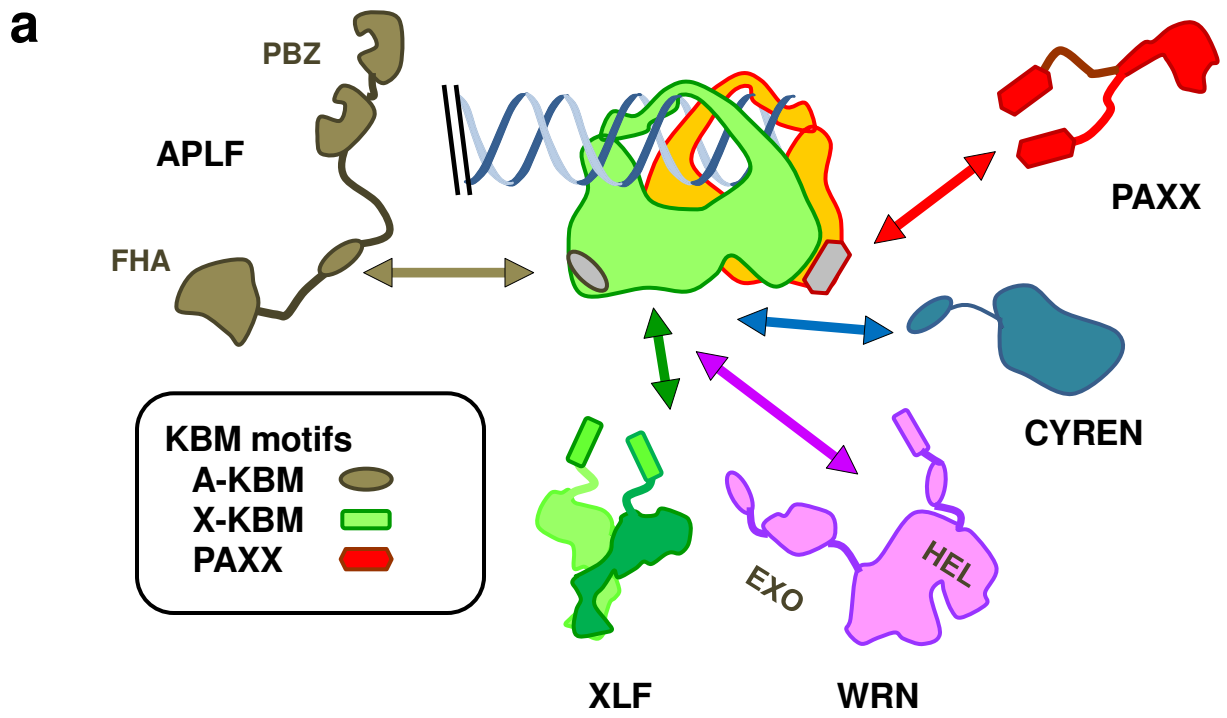

b APLF-like KBM motifs

APLF:

```
HUMAN   AERKRILPTWMLA
MOUSE   TQRKRILPAWMLA
CHICK   IQRRRVLPSWMLE
XENTR   VQRKRVLPDWMLH
DANRE   PLRKRVLPAWMTT
```

WRN-N:

```
HUMAN   TAQQRKCPEWMNV
MOUSE   TSLQRKFPEWMSM
CHICK   VDLQDKYPQWMCA
XENTR   TSLQRKLPEWMSV
DANRE   --GDRTLPKWMNN
```

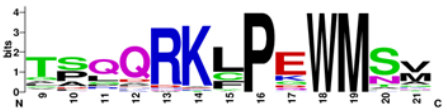

WRN-C1:

```
HUMAN   AERKRRLPVWFAK
MOUSE   SESKRKLPEWFAK
CHICK   PPGKRKVPAWFGA
XENTR   TTPKRKLPQWFGP
DANRE   QPAKRKLPDWTAG
```

MRI:

```
HUMAN     ETKTRVLPSWLTA
MOUSE     KTKTRVLPSWMTA
CHICK     AARRRLLPAWMGA
XENTR     KGKKRVLPEWMKE
DANRE     --KHRNLPQWMVK
```

c XLF-like KBM motifs

XLF:

```
HUMAN   SKVKRKKPRGLFS
MOUSE   VKSKRKKPRGLFS
CHICK   AKAKPKKAKGLFS
XENTR   SKPKKKKAKGLFT
DANRE   SRAKKKKAVGLFR
```

WRN-C2:

```
HUMAN   KLMDKTKRGGLFS
MOUSE   SSMAKTKKKGLFS
CHICK   KKPKADTRRGIFN
XENTR   KKAKTGKKKGIFD
DANRE   SEKRTKKKKGLFS
```

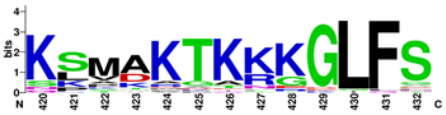

d PAXX KBM motifs

PAXX:

```
HUMAN     PGPGVRRRCPGESLINPGFKSKKPAGGVDFDE
MOUSE     SGPGVRRRCPGESLINPGFKSKKPAAGVDFDE
CHICK     SALPVKRKIPGESLINPGFKSKSVPSGVDFED
XENTR     SASQLKKRLPGESLINPGSKSKKAARGVDFEE
DANRE     PVVAVKKRLPGDSLINPGTKRKKPATGVAFDD
```

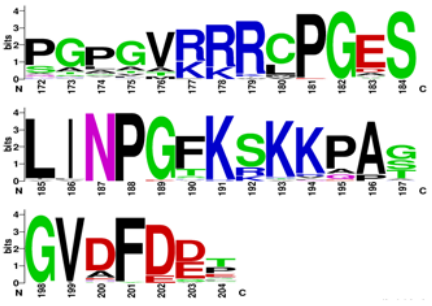

Supplementary Figure 1

(a) Scheme of the interactions between Ku70-Ku80 and the NHEJ factors containing an A-KBM (APLF, CYREN), an X-KBM (XLF) and both KBMs (WRN). The interaction of PAXX with Ku70 through its C-terminus is also represented. **(b-d)** Logo motif of the A-KBM, X-KBM and PAXX motifs obtained from multiple sequences alignment of these proteins as indicated (Crooks, G.E. *et al.*, WebLogo: a sequence logo generator. Genome Res 14, 1188-90 (2004)).

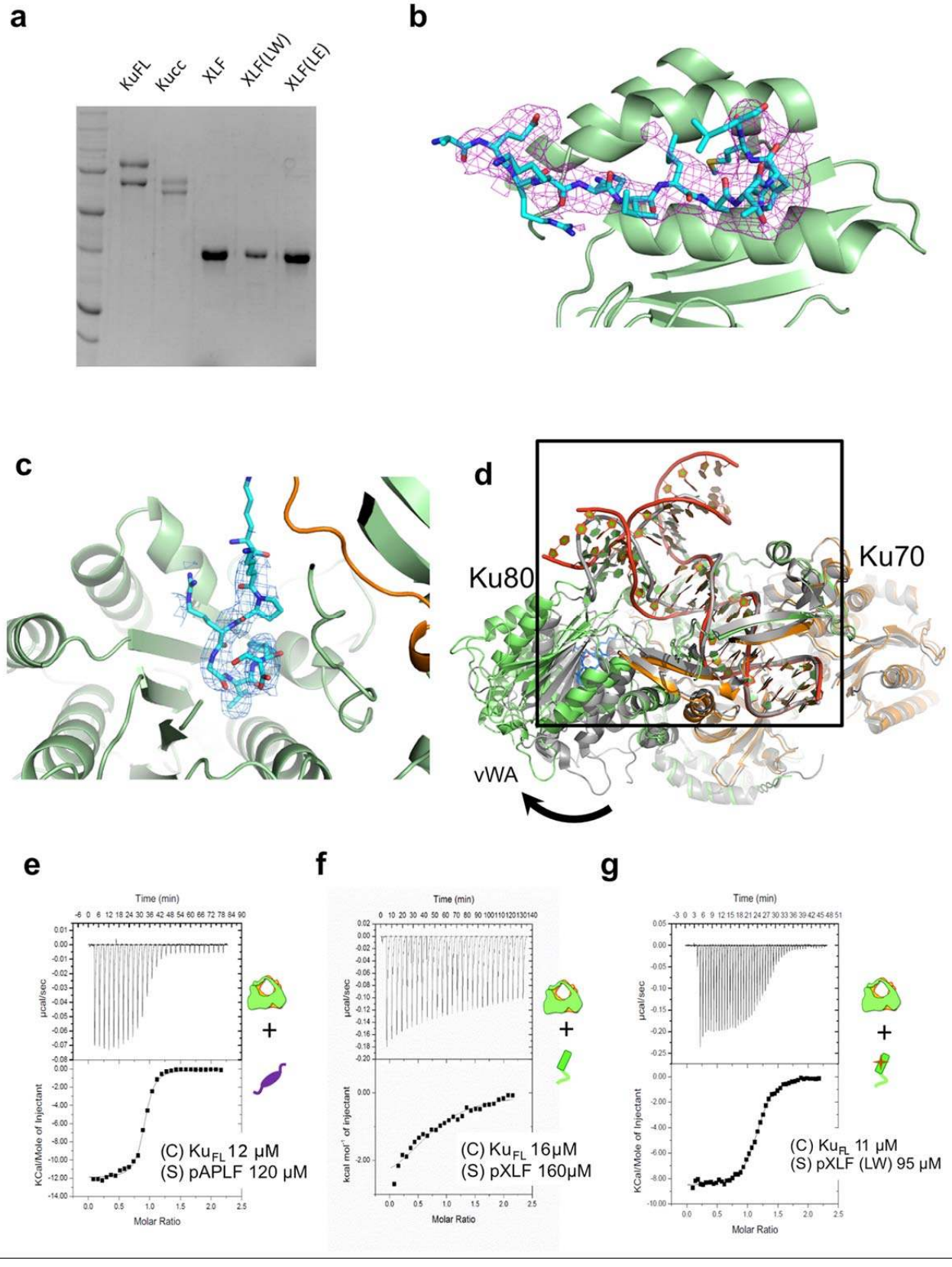
a
KuFL
Kucc
XLF
XLF(LW)
XLF(LE)
b
c
d
Ku80
Ku70
vWA
e
Time (min)
µcal/sec
KCal/Mole of Injectant
Molar Ratio
(C) Ku$_{FL}$ 12 µM
(S) pAPLF 120 µM
f
Time (min)
µcal/sec
kcal mol^{-1} of injectant
Molar Ratio
(C) Ku$_{FL}$ 16µM
(S) pXLF 160µM
g
Time (min)
µcal/sec
KCal/Mole of Injectant
Molar Ratio
(C) Ku$_{FL}$ 11 µM
(S) pXLF (LW) 95 µM

Supplementary Figure 2

(a) SDS gel showing purified Ku and XLF proteins as indicated. FL: full-length; cc: C-terminal truncation. **(b)** Electron density of peptide pAPLF. **(c)** Electron density of peptide pXLF. (**c**) DNA interactions with Ku in presence of X-KBM of XLF. Ku70-Ku80-hDNA-X-KBM (colored) compared to Ku70/Ku80/hDNA (PDB 1JEY, grey). Front view of Ku70-Ku80-hDNA-X-KBM showing the major deviation of hDNA molecules because of the conformational change of Ku80. (**d-e**) ITC analyses: representative thermograms and isotherms of titration corresponding to selected measurements from Table 2, as indicated.

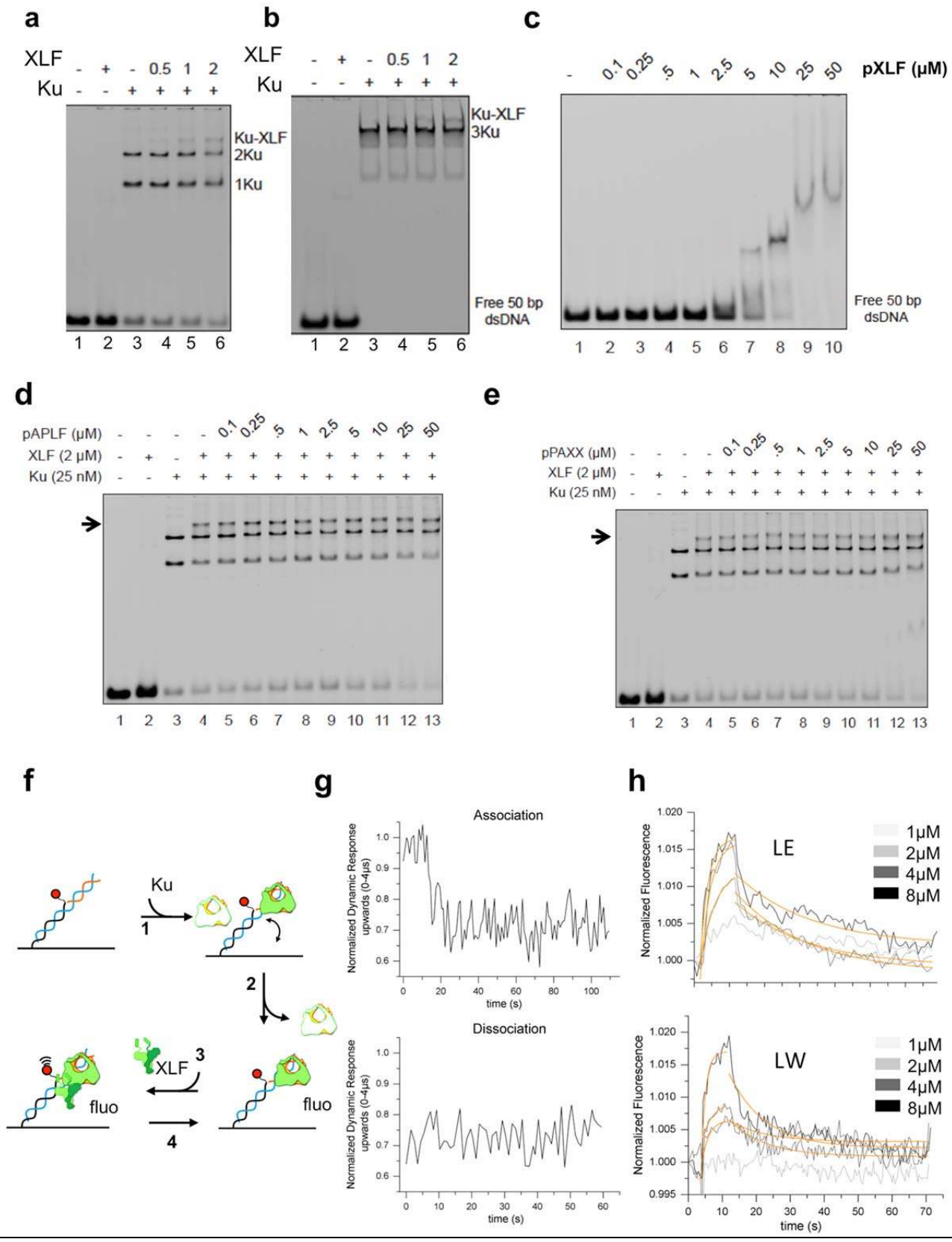
a
XLF
Ku
Ku-XLF
2Ku
1Ku
1 2 3 4 5 6
b
XLF
Ku
Ku-XLF
3Ku
Free 50 bp
dsDNA
1 2 3 4 5 6
c
pXLF (μM)
Free 50 bp
dsDNA
1 2 3 4 5 6 7 8 9 10
d
pAPLF (μM)
XLF (2 μM)
Ku (25 nM)
1 2 3 4 5 6 7 8 9 10 11 12 13
e
pPAXX (μM)
XLF (2 μM)
Ku (25 nM)
1 2 3 4 5 6 7 8 9 10 11 12 13
f
Ku
1
2
XLF
3
4
fluo
fluo
g
Association
Normalized Dynamic Response upwards (0-4μs)
time (s)
Dissociation
Normalized Dynamic Response upwards (0-4μs)
time (s)
h
LE
LW
1μM
2μM
4μM
8μM
Normalized Fluorescence
time (s)

Supplementary Figure 3

(a-e) EMSA analyses: (a, b) Gel shift assays with XLF and Ku at 20nM (a) or 200nM concentrations (b) in presence of a 50bp DNA with a FAM in 5'. **(c)** pXLF interaction with DNA as a control of the competition experiment in Figure 2e. **(d-e)** The pAPLF and PAXX Cter do not compete with the Ku-XLF complex. **(f-h) switchSENSE analyses: (f)** Scheme of the switchSENSE measurement flow: 1) Ku is bound to an 80bp nanolever with a fluorescent probe at position 48; 2) A washing step removes non-specifically bound Ku molecules; 3) XLF is then injected for real-time associations and dissociations at different concentrations followed by normalized changes in the fluorescence. **(g)** Binding kinetics of the Ku protein on the 80mer double-stranded DNA prior to the interaction with XLF, shown as changes in the dynamic response upwards (between 0 and 4µs). The dynamic response reflects the speed of the switching DNA, which decreases upon binding of the Ku analyte. The dissociation is represented only for one minute, to show that no dissociation of Ku from the DNA occurs while the XLF kinetics is measured. **(h)** Kinetic analyses of (LW) and (LE)XLF interactions. Solid grey lines represent raw data (from 1 to 8 µM; light grey to dark grey; averages of triplicates). Global fitting was performed, following a single-exponential function (solid orange lines) yielding kinetic rate constants; k_{ON} = 4.9 ± 0.5 10^4 $M^{-1}s^{-1}$ and k_{OFF} = 4.8 ± 0.5 10^{-2} s^{-1} for XLF(LE) and k_{ON} = 1.9 ± 1.1 10^5 $M^{-1}s^{-1}$and k_{OFF} = 8.4 ± 0.6 10^{-2} s^{-1} for XLF(LW).

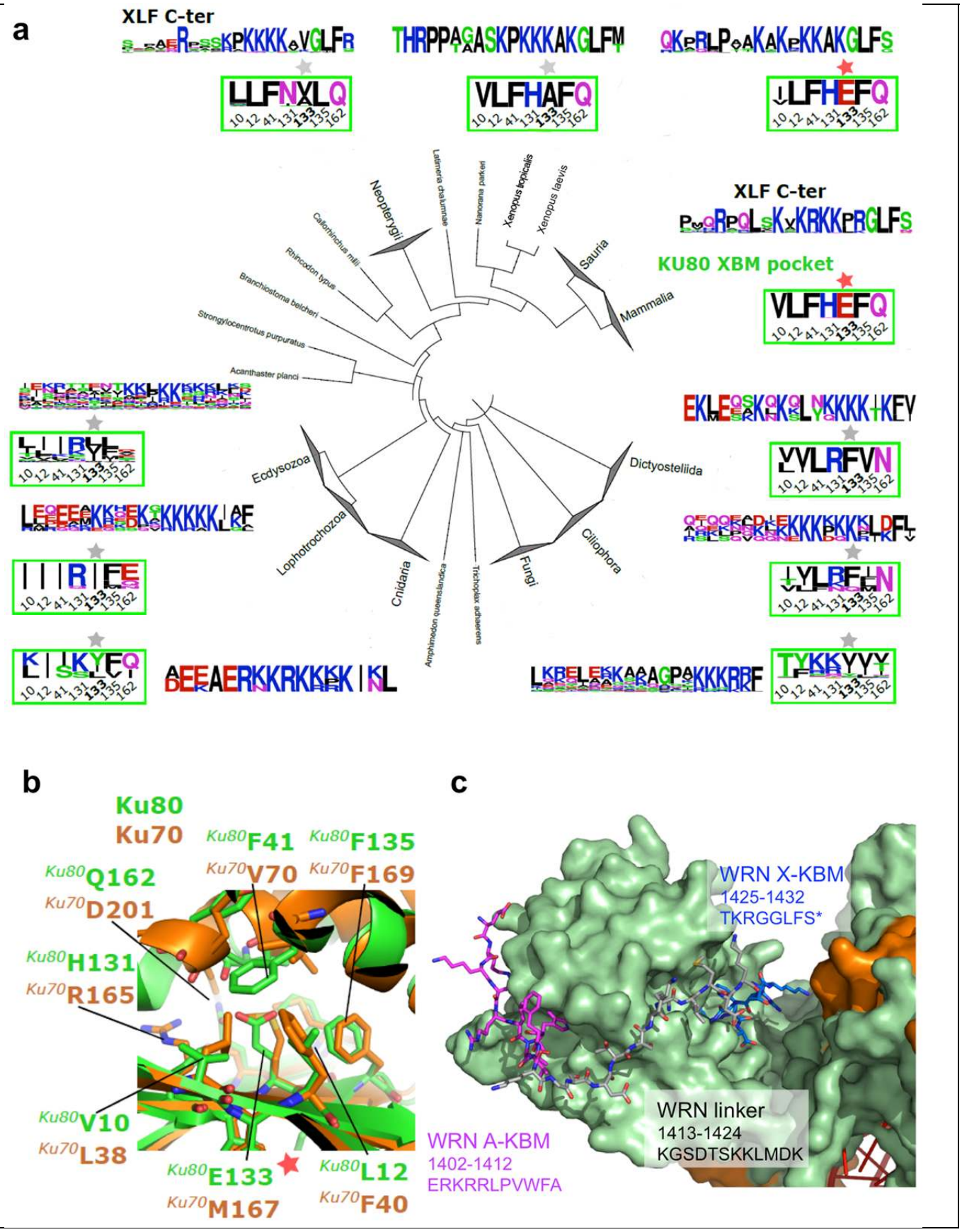
a
XLF C-ter
KU80 XBM pocket
Neopterygii
Sauria
Mammalia
Dictyosteliida
Ciliophora
Fungi
Cnidaria
Lophotrochozoa
Ecdysozoa
Latimeria chalumnae
Nanorana parkeri
Xenopus tropicalis
Xenopus laevis
Callorhinchus milii
Rhincodon typus
Branchiostoma belcheri
Strongylocentrotus purpuratus
Acanthaster planci
Amphimedon queenslandica
Trichoplax adhaerens
b
Ku80
Ku70
Ku80F41
Ku80F135
Ku80Q162
Ku70V70
Ku70F169
Ku70D201
Ku80H131
Ku70R165
Ku80V10
Ku70L38
Ku80E133
Ku80L12
Ku70M167
Ku70F40
c
WRN X-KBM
1425-1432
TKRGGLFS*
WRN linker
1413-1424
KGSDTSKKLMDK
WRN A-KBM
1402-1412
ERKRRLPVWFA

Supplementary Figure 4

(a) Variations among the sequence motifs observed for the C-terminal tail of XLF and for the seven positions of the Ku80 XBM pocket in various clades of the eukaryotic phylogenetic tree. 10 clades are represented summarizing the properties of 60 Mammalia, 36 Sauria, 31 Neopterygii, 62 Ecdysozoa, 9 Lophotrochozoa, 5 Cnidaria, 150 Fungi, 5 Ciliophora and 4 Dictyostellida sequences of XLF and Ku80. For each clade, web logos of the last 25 C-terminal amino-acids of XLF sequences are represented on top and the web logo of the X-KBM site positions is squared in green. A red star indicates the clades in which the position of Ku80 E133 was conserved as an acidic residue whereas a grey star points out that the acidic character of the residue was not maintained and was generally switched to a hydrophobic residue as observed in Ku70. **(b)** Superimposition of human Ku70 and Ku80 structures (PDB: 1JEQ) colored in orange and green, respectively, and focused on the region surrounding Ku80 E133 position in the X-KBM site. The red star points out the location of Ku80E133. Residues labelled and shown as sticks are the spatial neighbours of Ku80 E133. The side chain of Ku80 E133 is buried in the hydrophobic core of Ku80 and is not involved in any hydrogen bond or salt-bridge interaction resulting in a predicted pKa above 9.1 in the absence of XLF. **(c)** Molecular modelling of the interaction between Ku80 and the C-terminus of WRN containing an A-KBM in tandem with a X-KBM. The position of WRN motifs were deduced from the crystal structures presented here with APLF and XLF KBMs. The orientation of the KBMs and the size of the linker between WRN KBMs are compatible with a simultaneous binding of both WRN motifs to Ku80.

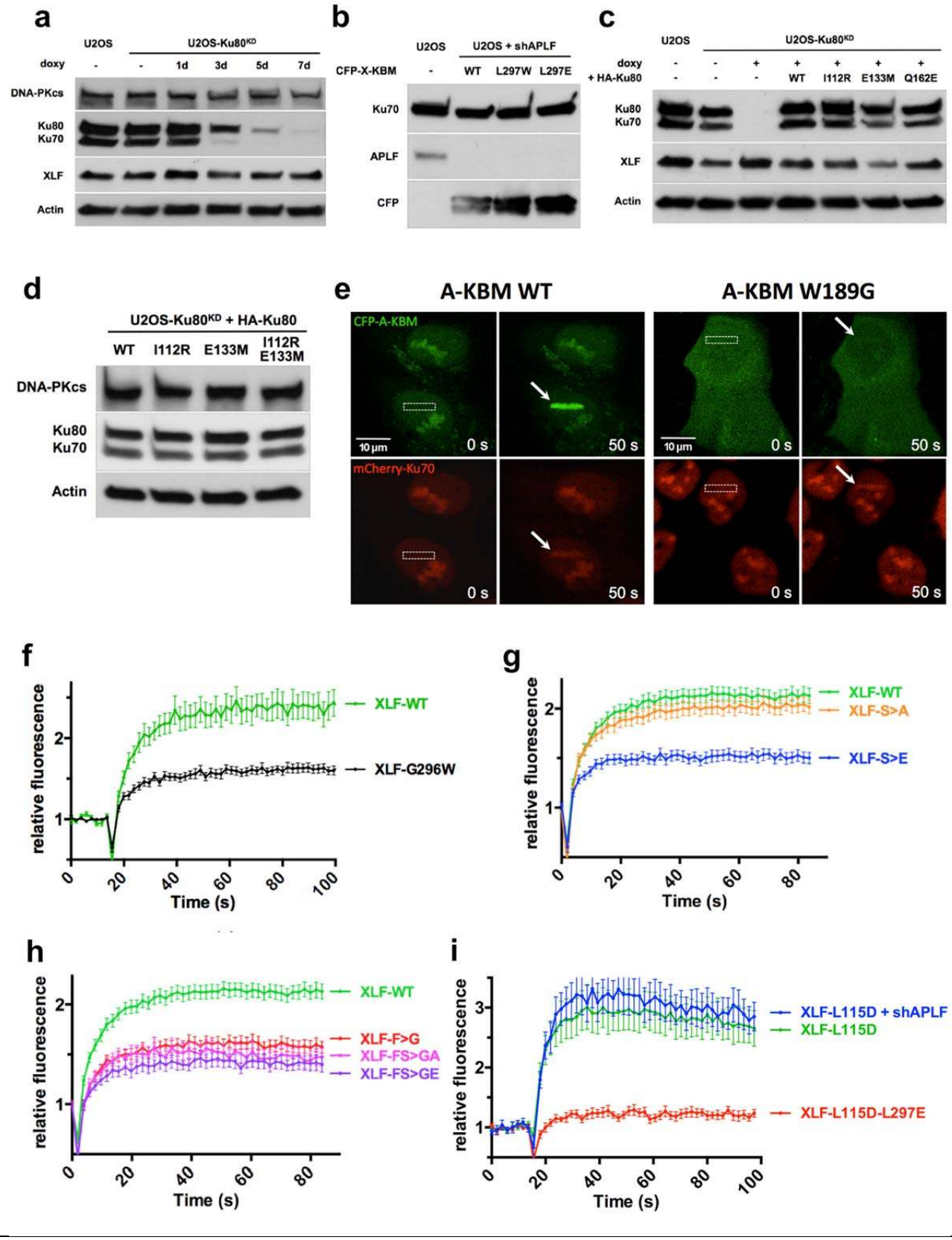
a
U2OS
U2OS-Ku80KD
doxy
-
-
1d
3d
5d
7d
DNA-PKcs
Ku80
Ku70
XLF
Actin
b
U2OS
U2OS + shAPLF
CFP-X-KBM
-
WT
L297W
L297E
Ku70
APLF
CFP
c
U2OS
U2OS-Ku80KD
doxy
+ HA-Ku80
-
-
+
+
+
+
+
-
-
-
WT
I112R
E133M
Q162E
Ku80
Ku70
XLF
Actin
d
U2OS-Ku80KD + HA-Ku80
WT
I112R
E133M
I112R
E133M
DNA-PKcs
Ku80
Ku70
Actin
e
A-KBM WT
A-KBM W189G
CFP-A-KBM
mCherry-Ku70
10 μm
0 s
50 s
f
relative fluorescence
Time (s)
XLF-WT
XLF-G296W
g
relative fluorescence
Time (s)
XLF-WT
XLF-S>A
XLF-S>E
h
relative fluorescence
Time (s)
XLF-WT
XLF-F>G
XLF-FS>GA
XLF-FS>GE
i
relative fluorescence
Time (s)
XLF-L115D + shAPLF
XLF-L115D
XLF-L115D-L297E

Supplementary Figure 5

(a-d) Western blot of U2OS cell extracts. **(a)** Whole cell extracts of U2OS shKu80 (U2OS-Ku80^{KD}) cells treated with doxycyclin for the indicated time were denatured and separated on 10% SDS-PAGE gel followed by electrotransfer on membrane. The membranes were blotted with the antibodies as indicated. **(b)** Whole cell extracts of U2OS shAPLF cells expressing WT or mutant CFP-X-KBM as indicated were processed as in (a). **(c)** Whole cell extracts of U2OS-Ku80^{KD} cells treated with doxycyclin for 7 days and expressing WT or mutant HA-Ku80 as indicated were processed as in (a). **(d)** Whole cell extracts of U2OS-Ku80^{KD} cells treated with doxycyclin for 7 days and expressing WT or mutant HA-Ku80 as indicated were processed as in (a). Uncropped blot images are shown in Supplementary Data Set 1. **(e)** Wild-type (WT) or mutant CFP-(A-KBM) and mCherry-Ku70 simultaneous behaviour after 800 nm pulsed-laser nuclear micro-irradiation assessed in U2OS cells by live cell-imaging at 0 s and 50 s post-irradiation. The white rectangle and arrows mark irradiated areas. **(f-h)** Dynamics of wild-type (WT) and mutant CFP-tagged full-length XLF at laser-damaged sites in BuS cells. Images were obtained at 1.94 s intervals and fluorescence intensities at the damage sites and in undamaged area were quantified. Mean values of the relative fluorescence with SEM were calculated from 20 independent measurements for each of WT and G296W XLF in (f), from 45, 40 and 20 independent measurements for each of WT, S299A and S299E XLF in (g) and from 45, 36, 20 and 20 independent measurements for each of WT, F298G, F298G/S299A, and F298G/S299E XLF in (h), respectively. *p* values at last time point: (f) WT vs G296W $p<0.0001$; (g) WT vs S>A $p=0.2785$; WT vs S>E $p<0.0001$. (h) WT vs F>G $p<0.0001$; WT vs FS>GA $p<0.0001$; WT vs FS>GE $p<0.0001$. **(i)** Dynamics of L115D and L115D/L233E CFP-tagged full-length mutant XLF at laser-damaged sites in BuS cells as in (f). Mean values of the relative fluorescence with SEM were calculated from 11 independent measurements for each of L115D±shAPLF and L115D/L233E XLF conditions. *p* values at last time point: L115D vs L115D±shAPLF $p=0.6113$; L115D vs L115D/L233E $p=0.0002$.

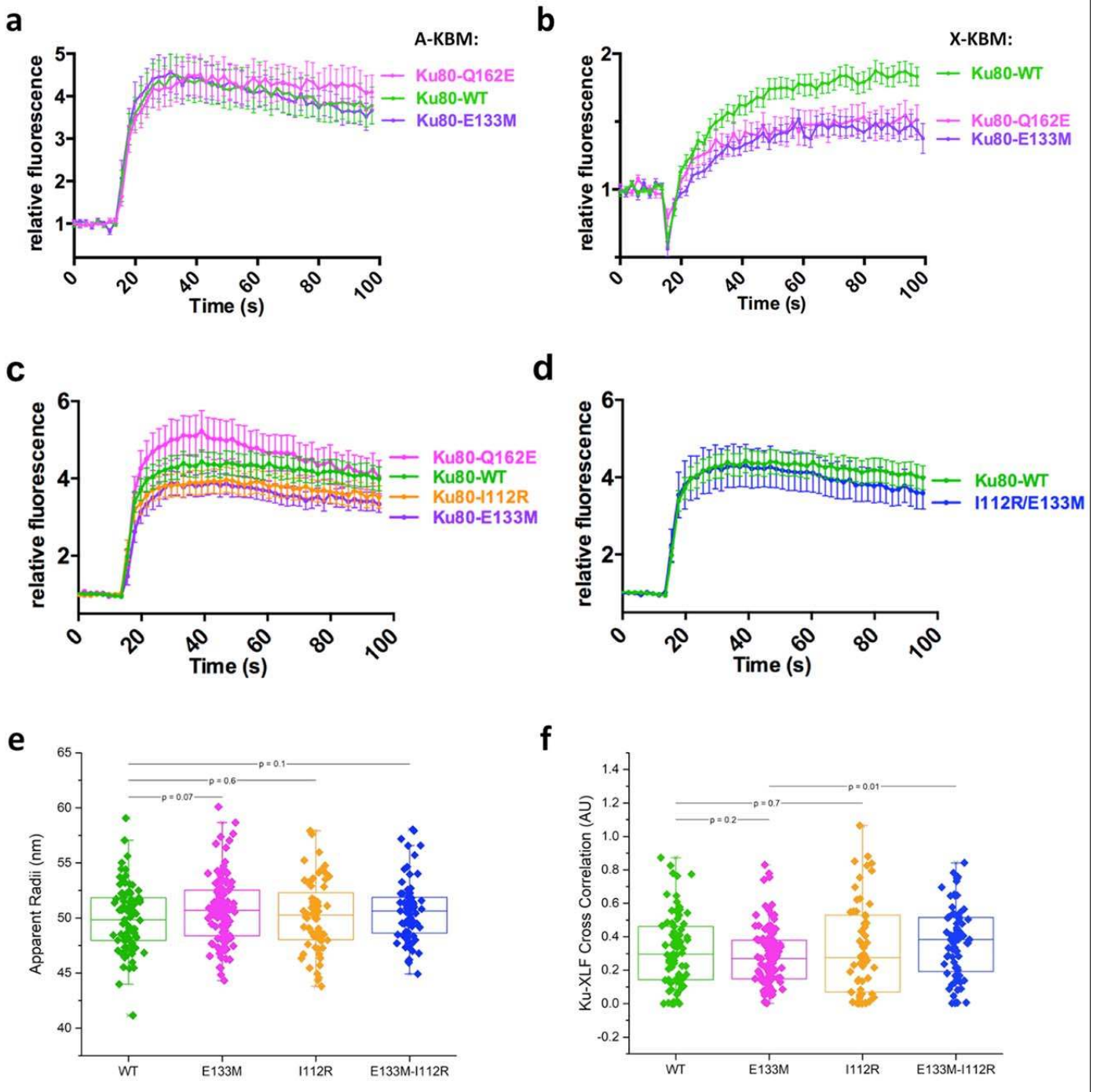

Supplementary Figure 6

(a-b) Dynamics of CFP-(A-KBM) (a) and (X-KBM) (b) at laser damaged sites in U2OS cells expressing wild-type (WT), E133M or Q162E mutant Ku80 as in Figure 3 b). Mean values of the relative fluorescence with SEM were calculated from 20, 23 and 22 independent measurements for A-KBM with WT, E133M or Q162E mutant Ku80 in (a) and from 48, 29 and 29 independent measurements for X-KBM with WT, E133M or Q162E mutant Ku80 in (b), respectively. *p* values at last time point: (a) WT vs E133M p=0.831; WT vs Q162E p=0.59519; (b) WT vs E133M p=0.0003; WT vs Q162E p=0.0111. **(c-d)** Dynamics of wild-type (WT) and

mutant CFP-Ku80 at laser damaged sites in U2OS cells. Mean values of the relative fluorescence with SEM were calculated from 25, 24, 20 and 15 independent measurements for WT, I112R, E133M and Q162E mutant Ku80 in (c) and from 25 and 26 independent measurements for WT or I112R/E133M mutant Ku80 in (d), respectively. *p* values at last time point: (c) WT vs Q162E =0.9252; WT vs I112R *p*=0.2734; WT vs E133M *p*=0.1101. (d) WT vs I112R-E1333M *p*=0.5362. (**e-f**) Analysis of XLF foci in U2OS cells by super-resolution. (e) Statistics of XLF foci size: each plot represents the average XLF foci size (indicated as radius translated from the correlation radius) in one nucleus. Box's height displays the standard deviation with the mean value labelled in the middle. 87, 110, 64, and 79 nuclei were taken in account for WT, E133M, I112R, and E133M-I112R double-mutant, respectively. The *p*-values were obtained by the t-test; (f) Statistics of the Cross-Pair-Correlation between Ku and XLF: Ku and XLF were stained with antibodies labelled by different fluorophores (Alexa488 conjugated rabbit anti-Ku80, abcam198586, Alexa647 conjugated goat anti-mouse secondary + Mouse anti-XLF, NBP2-03275), and dual-colour super-resolution imaging was performed to examine the cross-correlation between Ku and XLF foci within each nucleus. Each plot represents the cross-correlation amplitude calculated across one nucleus. Box's height displays the standard deviation with the mean value labelled in the middle. 83, 107, 57, and 72 nuclei were taken in account for WT, E133M, I112R, and E133M-I112R mutants respectively. The *p*-value were obtained by the t-test.

Expression vectors

All lentiviral vectors derived from pLVTHM (Addgene plasmid #12247) and pLV-tTR-KRAB-Red (Addgene plasmid #12250) plasmids. Both were gifts from Didier Trono [1].

The pLVTHM2 vector was obtained by digesting pLVTHM with PmeI/SpeI and inserting the PBXS linker (i.e. preannealed PBXS-F/PBXS-R pair of oligonucleotides) in order to remove the GFP coding sequence. To generate lentiviral vectors for conditional expression of shRNA, pLVTHM2 was digested with MluI/ClaI and the following pairs of preannealed oligonucleotides were inserted by ligation: shKu80-F/shKu80-R (target sequence designed by Denis Biard, CEA-DSV, France, personal communication) or shAPLF-F/shAPLF-R (target sequence from [2]) to knockdown the expression of Ku80 or APLF, respectively.

The pLV-tTR-KRAB vector was obtained from pLV-tTR-KRAB-Red by replacing the DsRed coding sequence by the XBES linker at XmaI/SpeI restriction sites.

The pLV-Red vector derived from pLV-tTR-KRAB-Red by replacing the tTR-KRAB coding sequence by the PEKBBMX linker at PmeI/XmaI restriction sites.

The pLV3 vector derived from pLV-tTR-KRAB-Red through the following modifications: first, the NsiI/Kpn2I fragment was replaced by the nPNk linker. The tTR-KRAB coding sequence was then removed by PmeI/XmaI digestion and replaced by the PEKBBMX linker. Finally, the IRES-DsRed fragment was removed by PmeI/SpeI digestion and replaced by the PKXMBBES linker.

To express ECFP-tagged A-KBM (APLF P177 to E193) or X-KBM (XLF S287 to S299) motifs, the A-KBM linker or X-KBM linker, respectively, was inserted into the Acc65I/BamHI restriction sites of the pECFP-C1 plasmid (Clontech) and the AgeI/BamHI fragment (ECFP-A-KBM or ECFP-X-KBM) was subcloned into the Kpn2I/BamHI restriction sites of pLV3. The ECFP-tagged A-KBM-W189G, X-KBM-L297W and X-KBM-L297E expressing vectors were obtained by amplifying by PCR the corresponding cDNAs using the pECFP-A-KBM or pECFP-X-KBM plasmid as a template, as well as CMV-F as forward primer and Bam-A-KBM-W189G-R, XLF-L297W-Bam-R or XLF-L297E-Bam-R as reverse primer, respectively. The PCR fragments were digested with AgeI/BamHI and inserted into Kpn2I/BamHI restriction sites of pLV3.

To express full-length ECFP-tagged XLF protein, human XLF cDNA (a gift from Jean-Pierre de Villartay, Institut Imagine, Paris, France) was amplified by PCR using the XLF-Hind-F and XLF-Bam-R primers. The resulting PCR fragment was digested with HindIII/BamHI and inserted into pECFP-C1. The ECFP-XLF coding fragment was then excised with AgeI/BamHI and inserted into pLV3 at Kpn2I/BamHI restriction sites. ECFP-XLF-L297W, -L297E, -F298G, -S299A, -S299E, -F298G-S299A, and -F298G-S299E mutants were expressed by PCR amplification of the corresponding XLF coding sequences using the pECFP-XLF vector as a template, Kpn2-MCS-F as forward primer, and XLF-L297W-Bam-R, XLF-L297E-Bam-R, XLF-F298G-Bam-R, XLF-S299A-Bam-R, XLF-S299E-Bam-R, XLF-FS298GA-Bam-R, or XLF-FS298GE-Bam-R, as reverse primer, respectively. The resulting fragments were digested with Kpn2I/BamHI and inserted into pLV3-ECFP-XLF to replace the XLF wild-type coding sequence. The XLF-L115D coding sequence was obtained by overlapping PCR mutagenesis on pLV3-ECFP-XLF template using ECFP-Cter-F and XLF-Bam-R oligos as outer primers, and XLF-L115D-F and XLF-L115D-R as mutated inner primers. The PCR product (XLF-L115D) was then digested with Kpn2I/BamHI and inserted into pLV3-ECFP-XLF to replace the XLF-WT coding sequence. The XLF-L115D-L297E double mutant coding sequence was obtained as above, except that the XLF-Bam-R outer primer was replaced by XLF-L297E-Bam-R.

Lentiviral vectors expressing untagged full-length XLF proteins (WT, L297W or L297E) were obtained by subcloning Kpn2I/BamHI fragments from the respective pLV3-ECFP-XLF into the pLV-Red vector.

The ECFP-XRCC4 expressing vector was obtained by excision of a Kpn2I/BamHI fragment containing the XRCC4 coding sequence from the pEGFP-C1-FLAG-XRCC4 plasmid (gift from Steve Jackson (Addgene #46959), [3]). The resulting fragment was inserted into pLV3-ECFP-XLF to replace the XLF coding sequence.

To obtain shRNA-resistant human Ku80 expression vector, HA-Ku80 coding sequence was amplified by overlapping PCR from pICE-Puro-HA-Ku80 (a kind gift from Sébastien Britton, IPBS, Toulouse, France) with Kpn2-HA-F and pICE-Xba-R as outer primers, and Ku80-shRes-F and Ku80-shRes-R as inner primers that introduce silent mutations in the shRNA target sequence. The resulting fragment was then inserted into pLV3 after digestion with Kpn2I/MluI. The Ku80-L112R expressing pLV3 vector was constructed by overlapping PCR from pLV3-HA-Ku80-shR using pLV-F and pLV-R oligonucleotides as outer primers and Ku80-L112R-F and Ku80-L112R-R as mutated inner primers. The PCR product was then digested with Kpn2I/MluI and inserted into pLV3. Other Ku80 single mutant constructs

(E133M and Q162E) were obtained similarly by using the corresponding pairs of inner primers (Ku80-E133M-F/Ku80-E133M-R and Ku80-Q162E-F/Ku80-Q162E-R, respectively). The pLV3-HA-Ku80-shR-L112R-E133M double mutant expressing vector was obtained as above for the E133M single mutant construct, except that pLV3-HA-Ku80-shR-I112R was used as a template for PCR reactions.

Expression vectors for ECFP-tagged WT or mutants Ku80 were obtained by amplifying the ECFP coding sequence by PCR from the pECFP-C1 plasmid with the Pme-Koz-ECFP-F and pme-CFP-80-R primers. The PCR fragment was then inserted at the PmeI restriction site in the various pLV3-HA-Ku80-shR plasmids by use of the Hot-Fusion strategy [4].

To generate pLV3-mCherry-FLAG-Ku70 vector allowing expression of an mCherry-tagged Ku70 protein, the FLAG-Ku70 coding sequence was amplified by PCR using Kpn2-FLAG-F and Mlu-Ku70-R primers, digested with Kpn2I/MluI and cloned into pLV3. The mCherry coding sequence was then inserted at the PmeI restriction site by Hot-Fusion cloning [5] following PCR amplification using Pme-Koz-ECFP-F and Kpn2-pme-mCh-R primers and the pmCherry-C1-3NLS plasmid as a template (gift from Dyche Mullins (Addgene #58476), [6]).

The pLV3-Tet-RFP-ISceI-GRLBD lentiviral vector for conditional expression of I-SceI was prepared as follows : pLV3 was first modified by inserting at the PacI restriction site the Tet-Pac-F/Tet-Pac-R pre-annealed linker which contains two tetracyclin operator DNA elements. The resulting pLV3-Tet plasmid was then digested by Kpn2I/BamHI to receive the AgeI/BamHI fragment from the pISceI-GR-RFP plasmid (gift from Tom Misteli (Addgene #17654), [7]) which contains the coding sequence of DsRed-ISceI-GRLBD.

All oligonucleotides were purchased from Eurofins Genomics (Ebersberg, Germany). Restriction and modifying enzymes (Phusion and T4 DNA Ligase) were from ThermoFisher Scientific (Illkirch, France). All constructs were checked by sequencing (Eurofins Genomics).

Oligonucleotides used as linkers (alphabetical order; sequences 5' to 3')

A-KBM-F	GTACC CCA ATC CTT GCC GAG AGG AAA AGA ATC CTT CCA ACT TGG ATG TTA GCA GAA TAG
A-KBM-R	GATCCTA TTC TGC TAA CAT CCA AGT TGG AAG GAT TCT TTT CCT CTC GGC AAG GAT TGG G
nPNk-F	CTCCATCGATCGCCATGGTGA
nPNk-R	CCGGTCACCATGGCGATCGATGGAGTGCA

PBXS-F	AAAC CGTACG GATATC T CCCGGG TC A
PBXS-R	CTAGT GA CCCGGG A GATATC CGTACG GTTT
PEKBBMX-F	AAACTACGGGATC GAATTC CTCGCT TCCGGA CTTCGT GGATCC ACTCTC CGTACG ACTGCT ACGCGT ACTTCAC
PEKBBMX-R	CCGGGTGAAGT ACGCGT AGCAGT CGTACG GAGAGT GGATCC ACGAAG TCCGGA AGCGAG GAATTC GATCCCGTAGTTT
PKXMBBES-F	AAACTACGG GATC TCCGGA CACCTT CCCGGG TCACTC ACGCGT CTCATT GGATCC CGTACG GAATTC A
PKXMBBES-R	CTAGT GAATTC CGTACG GGATCC AATGAG ACGCGT GAGTGA CCCGGG AAGGTG TCCGGA GATC CCGTAGTTT
shAPLF-F	CGCGTCCCC GAA GAA ATC TGC AAA GAT A TTCAAGAGA T ATC TTT GCA GAT TTC TTC TTTTTGGAAAT
shAPLF-R	CGATTTCCAAAAA GAA GAA ATC TGC AAA GAT A TCTCTTGAA T ATC TTT GCA GAT TTC TTC GGGGA
shKu80-F	CGCGTCCCC G AAC AAG GAT GAG ATT GCT TTCAAGAGA AGC AAT CTC ATC CTT GTT C TTTTTGGAAAT
shKu80-R	CGATTTCCAAAAA G AAC AAG GAT GAG ATT GCT TCTCTTGAA AGC AAT CTC ATC CTT GTT C GGGGA
TetO-Pac-F	TCCCTATCAGTGATAGAGATCTCCCTATCAGTGATAGAGAAT
TetO-Pac-R	TCTCTATCACTGATAGGGAGATCTCTATCACTGATAGGGAAT
XBES-F	CCGGG GGATCC CTCGAG GAATTC A
XBES-R	CTAGT GAATTC CTCGAG GGATCC C
X-KBM-F	GTACC TCA AAG GTC AAG AGG AAG AAG CCA AGG GGT CTC TTC AGT TAG
X-KBM-R	GATCCTA ACT GAA GAG ACC CCT TGG CTT CTT CCT CTT GAC CTT TGA G

Oligonucleotides used as PCR primers (alphabetical order; sequences 5' to 3')

Bam-A-KBM-W189G-R	CGTACGGGATC CTA TTC TGC TAA CAT CCC AGT TGG AAG GAT TCT TTT CCT C
CMV-F	GTAGGCGTGTACGGTGGGAGG
ECFP-Cter-F	C ATG GTC CTG CTG GAG TTC GTG
Kpn2-HA-F	CTCTGC TCCGGA GCCACC ATG TAC CCC TAC GAT GTG C
Kpn2-FLAG-F	CTCTCGTCCGGAGCCGCACC ATG GAC TAC AAG GAT G
Kpn2-MCS-AKF-F	CTCGCTTCCGGACTCAGATCTCGAGCTC
Kpn2-pme-mCh-R	GGTGCGGCTCCGGAGATCCCGTAGTTTGGACTTGTACAGCTCGTCCATGCCG
Ku80-E133M-F	GAG GCA TAT TAT GAT ATT CAC TGA CCT CAG CAG CCG ATT C
Ku80-E133M-R	GGT CAG TGA ATA TCA TAA TAT GCC TCT TCT CAA ACT TCT TTC CTA TTG
Ku80-I112R-F	C TTC CTG GAT GCA CTA AGA GTG AGC ATG GAT GTG ATT CAA C
Ku80-I112R-R	G AAT CAC ATC CAT GCT CAC TCT TAG TGC ATC CAG GAA GTC
Ku80-Q162E-F	CAT CTC CCT GGA ATT CTT CTT GCC TTT CTC ACT TGG C

Ku80-Q162E-R	GGC AAG AAG AAT TCC AGG GAG ATG TCA CAT TTC TTC AAG C
Ku80-shRes-F	GCT GAA AAT AAA GAC GAA ATC GCC TTA GTC CTG TTT GGT ACA GAT GGC
Ku80-shRes-R	GAC TAA GGC GAT TTC GTC TTT ATT TTC AGC AAA CAC CTG TCG CTG TAC
Mlu-Ku70-R	CTCTGCACGCG TCA GTC CTG GAA GTG CTT GGT GAG GGC
pICE-Xba-R	CAGCGGGTTTA TCTAGA CTGCAG ACGCGT GC
pLV-F	CCGATCACGAGACTAGCCTCGAGG
pLV-R	CCAGTCAATCTTTCACAAATTTTGTAATCCAGAGG
pme-CFP-80-R	CATGGTGGCTCCGGAGATCCCGTAGTTTGACTTGTACAGCTCGTCCATGCCG
Pme-Koz-CFP-F	CGATCACGAGACTAGCCTCGAGGTTTAAACGCCGCCACCATGGTGAGCAAGG GC
XLF-Bam-R	CTCTC GGATC CTA ACT GAA GAG ACC CCT TGG CTT CTT CCT CTT GAC C
XLF-F298G-Bam-R	CTCTC GGATC CTA ACT GCC GAG ACC CCT TGG CTT CTT CCT CTT GAC C
XLF-FS298GA-Bam-R	CTCTCGGATC CTA AGC GCC GAG ACC CCT TGG CTT CTT CCT CTT GAC C
XLF-FS298GE-Bam-R	CTCTCGGATC CTA CTC GCC GAG ACC CCT TGG CTT CTT CCT CTT GAC C
XLF-Hind-F	CTCTCAAGCTTCCGCCACC ATG GAA GAA CTG GAG CAA GGC CTG
XLF-L115D-F	G CGA AGT GAG CTC TCT GGC GAC CCC TTC TAT TGG AAT TTC C
XLF-L115D-R	G GAA ATT CCA ATA GAA GGG GTC GCC AGA GAG CTC ACT TCG C
XLF-L297E-Bam-R	CTCTC GGATC CTA ACT GAA CTC ACC CCT TGG CTT CTT CCT CTT GAC C
XLF-L297W-Bam-R	CTCTC GGATC CTA ACT GAA CCA ACC CCT TGG CTT CTT CCT CTT GAC C
XLF-S299A-Bam-R	CTCTCGGATC CTA AGC GAA GAG ACC CCT TGG CTT CTT CCT CTT GAC C
XLF-S299E-Bam-R	CTCTCGGATC CTA CTC GAA GAG ACC CCT TGG CTT CTT CCT CTT GAC C

References

1. Wiznerowicz, M. & Trono, D. Conditional suppression of cellular genes: lentivirus vector-mediated drug-inducible RNA interference. *J Virol* **77**, 8957-61 (2003).
2. Iles, N., Rulten, S., El-Khamisy, S.F. & Caldecott, K.W. APLF (C2orf13) is a novel human protein involved in the cellular response to chromosomal DNA strand breaks. *Mol Cell Biol* **27**, 3793-803 (2007).
3. Britton, S., Coates, J. & Jackson, S.P. A new method for high-resolution imaging of Ku foci to decipher mechanisms of DNA double-strand break repair. *J Cell Biol* **202**, 579-95 (2013).
4. Fu, C., Donovan, W.P., Shikapwashya-Hasser, O., Ye, X. & Cole, R.H. Hot Fusion: an efficient method to clone multiple DNA fragments as well as inverted repeats without ligase. *PLoS ONE* **9**, e115318 (2014).

5. Frit, P., Barboule, N., Yuan, Y., Gomez, D. & Calsou, P. Alternative end-joining pathway(s): Bricolage at DNA breaks. *DNA Repair (Amst)* **17**, 81-97 (2014).
6. Belin, B.J., Lee, T. & Mullins, R.D. DNA damage induces nuclear actin filament assembly by Formin -2 and Spire-(1/2) that promotes efficient DNA repair. [corrected]. *Elife* **4**, e07735 (2015).
7. Soutoglou, E. et al. Positional stability of single double-strand breaks in mammalian cells. *Nat Cell Biol* **9**, 675-82. (2007).

Uncropped image related to Figure 2e

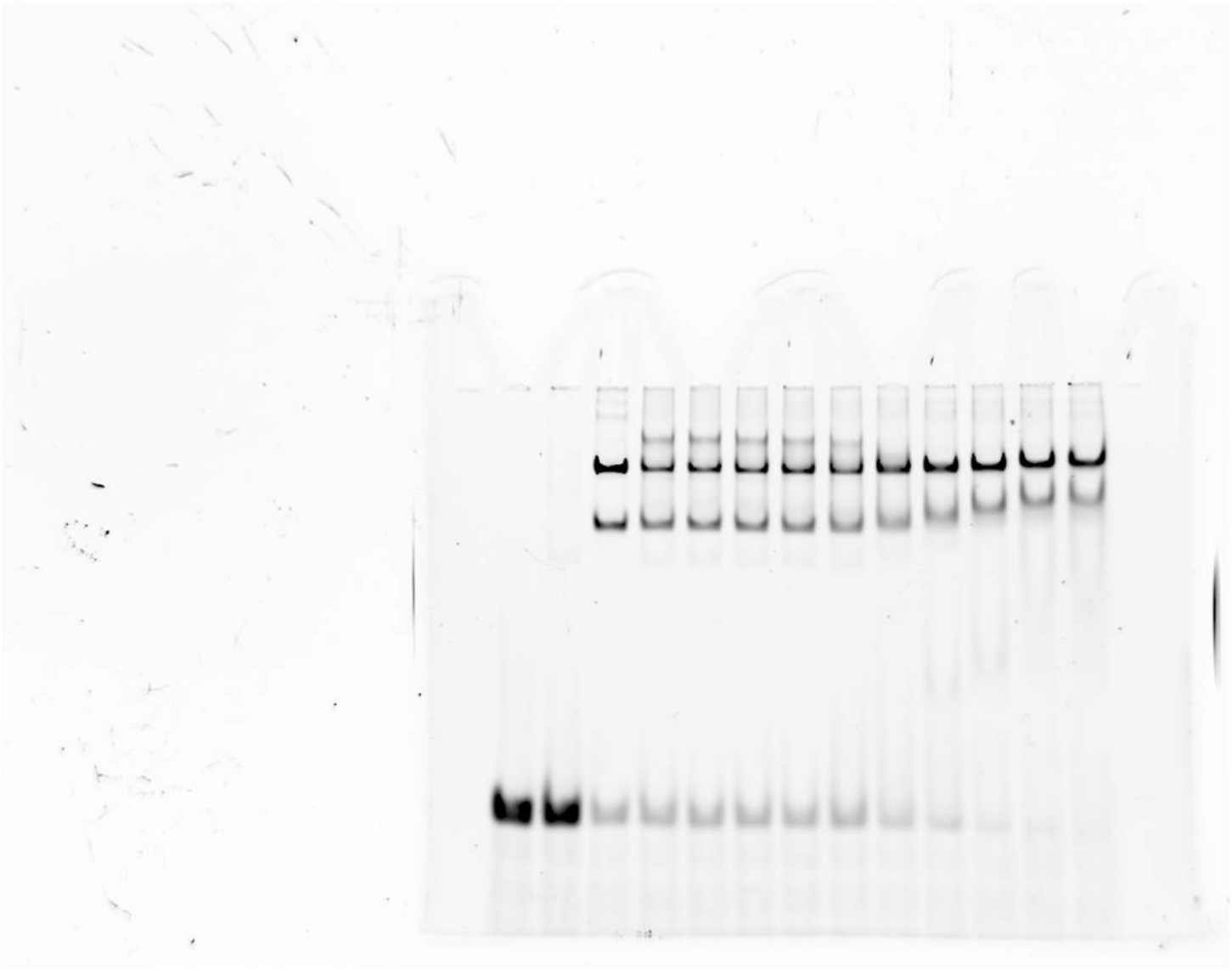

Uncropped scans related to Suppl. Fig. 5a-d